

Chapter 5

Experimental results

In this chapter we present the experimental results that we obtained when testing the methods proposed in this thesis.

In section 5.1, we present experimental results related to the geometrical (un)distortion model proposed in section 3.1. We show that the geometrical distortion introduced by the Image Intensifier can be accurately modeled by a polynomial of the view parameters. Also, we show that the estimated polynomial is independent of the focal length, but not for changes of anatomical angles. For each polynomial of the (un)distortion model, we estimate its optimal degree. Moreover, we prove that by decomposing the polynomial in two components, namely the steady and the orientation-dependent one, the optimal degree of the polynomial, describing the orientation-dependent components, reduces and, therefore, the estimation of this polynomial from the anatomical angles α and β is simplified. We also give experimental data relating the accuracy obtained using this model.

Section 5.2 is devoted to the assessment of the performance of each of the models proposed in section 3.2 to estimate the acquisition geometry, described by the extrinsic parameters \mathbf{R} and \mathbf{t} . First, we present results of the accuracy obtained when calibrating the acquisition geometry using Zhang's method. Afterwards, and using a subset of the obtained extrinsic parameters and the corresponding anatomical angles, we estimate the parameters of each of the proposed models in section 3.2. Finally, we test the accuracy of each model by projecting the grid on the images using the extrinsic parameters estimated by each model and comparing the position of the grid nodes with the real ones.

After calibrating the system, we can focus on the three-dimensional reconstruction. Hence, in section 5.3, first we compare the obtained three-dimensional reconstruction accuracy using biplane snakes to the obtained with manual reconstruction. Second, we study the biplane snakes performance when approaching the reconstruction of wavy vessels, and we evaluate the influence of image distortion on the 3D reconstruction accuracy. Afterwards, we use real images to test 3D reconstruction accuracy when using biplane snakes and some practical issues relating the biplane snakes. Finally, we present some examples of the application of the proposed techniques to the three-dimensional reconstruction of vessels from real cardiac images.

All the experiments presented in this chapter using real images were performed with a SIEMENS Cathcor 3.3 C-arm angiography acquisition system in the University Hospital "Germans Trias i Pujol" (Badalona, Spain).

5.1 Geometrical (Un)Distortion Model

Following the distortion model proposed in section 3.1, we can obtain the distorted coordinates (\hat{u}, \hat{v}) of a point (u, v) in a view acquired with rotation angle α and angulation angle β by the following expression:

$$\begin{aligned}\hat{u} &= u + \bar{\rho}^u(u, v) + \delta^u(u, v, \alpha, \beta) \\ \hat{v} &= v + \bar{\rho}^v(u, v) + \delta^v(u, v, \alpha, \beta)\end{aligned}$$

where

$$\begin{aligned}\delta^u(u, v, \alpha, \beta) &= \sum_{n=0}^N \sum_{m=0}^n \omega^{u,j}(\alpha, \beta) u^{n-m} v^m = \delta_{\alpha, \beta}^u(u, v) \\ \delta^v(u, v, \alpha, \beta) &= \sum_{n=0}^N \sum_{m=0}^n \omega^{v,j}(\alpha, \beta) u^{n-m} v^m = \delta_{\alpha, \beta}^v(u, v)\end{aligned}$$

with $j = \frac{n(n+1)}{2} + m$ and N is the polynomial degree of $\delta_{\alpha, \beta}^u(u, v)$ and $\delta_{\alpha, \beta}^v(u, v)$

We can, therefore, distinguish three groups of polynomials in this model:

- First, the polynomials of (u, v) describing the steady component of distortion, $\bar{\rho}^u(u, v), \bar{\rho}^v(u, v)$.
- Second, the polynomials of (u, v, α, β) describing the orientation-dependent component, $\delta^u(u, v, \alpha, \beta), \delta^v(u, v, \alpha, \beta)$. These polynomials are defined as bi-variate polynomials of (u, v) , namely $\delta_{\alpha, \beta}^u(u, v), \delta_{\alpha, \beta}^v(u, v)$, whose coefficients are bi-variate polynomials of (α, β) . We denote the polynomial that estimates the j th coefficient of polynomial $\delta_{\alpha, \beta}^u(u, v)$ as $\omega^{u,j}(\alpha, \beta)$.
- The third group of polynomials is therefore formed by the sets of polynomials $\{\omega^{u,j}(\alpha, \beta)\}$ and $\{\omega^{v,j}(\alpha, \beta)\}$, for $j = 1 \dots M$, where M is the number of coefficients of the bi-variate polynomials $\delta_{\alpha, \beta}^u(u, v)$ and $\delta_{\alpha, \beta}^v(u, v)$.

The undistortion model is analogously constructed.

Our aim is first determining if such a polynomial model is accurate to model the geometrical distortion. Also, we aim proving that geometrical distortion is only affected by the orientation of the detector, and not by the focal length. Finally, we empirically determine the optimal degree for each of these polynomials, and determine the accuracy obtained by the optimal configuration for the proposed model.

5.1.1 Polynomial Suitability to Model Geometrical Distortion

With this experiment, we aim to assess two issues: First, whether a bivariate polynomial is suitable to accurately describe the geometrical distortion for a given view. Second, if it is suitable, which would be the optimal degree for this polynomial.

To this aim, we acquired images of the calibration grid at 25 different orientations of the Image Intensifier, namely for $\alpha = [-30, 0, 30, 60, 90]$ and $\beta = [20, 10, 0, -10, 20]$. We chose these values since they cover the range used in clinical practice at the University Hospital "Germans Trias i Pujol". For each image, about 150 crossing points (\hat{u}, \hat{v}) were detected, and corresponding ideal pixel coordinates (u, v) were estimated. Then, we randomly divided the crossing points into two sets for each image: 50% of crossing points for estimation and 50% for test. Let $[\hat{\mathbf{u}}_k^c, \hat{\mathbf{v}}_k^c]$, $[\mathbf{u}_k^c, \mathbf{v}_k^c]$, be the distorted and undistorted coordinates of the crossing points in the calibration set for each view k . Analogously, for the test set we have $[\hat{\mathbf{u}}_k^t, \hat{\mathbf{v}}_k^t]$ and $[\mathbf{u}_k^t, \mathbf{v}_k^t]$.

For each view k , we used the estimation set of points to fit the bi-variate polynomials $\rho_k^u(u, v)$ and $\rho_k^v(u, v)$ to the distortion, namely to $\hat{\mathbf{u}}_k^c - \mathbf{u}_k^c$ and $\hat{\mathbf{v}}_k^c - \mathbf{v}_k^c$. We followed this procedure for different polynomial degrees, ranging from 1 to 9. Then, we evaluated the performance of each polynomial for both sets of points, the calibration and the test.

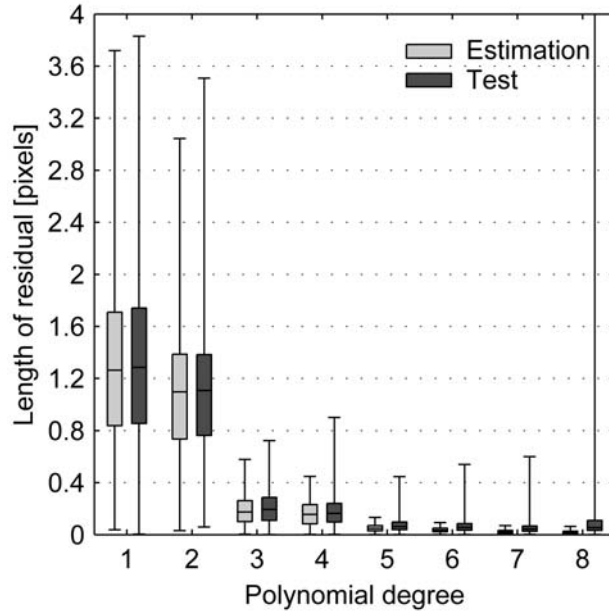
Figure 5.1(a) shows the obtained results. A polynomial of degree greater than 5 does not improve the precision on test points. Indeed, a polynomial of degree greater than 5 deteriorates the precision on test points, since the polynomial model is *learning* the error of feature estimate. This fact was already reported in [91] in the frame of camera calibration. Thus, for the distortion model we have chosen a polynomial of degree 5, expecting a mean error of less than 0.1 pixels, achieving subpixel accuracy.

We proceeded in the same way for the undistortion polynomials $\rho_k^{\hat{u}}(\hat{u}, \hat{v})$ and $\rho_k^{\hat{v}}(\hat{u}, \hat{v})$, which were fitted to $\mathbf{u}_k^c - \hat{\mathbf{u}}_k^c$ and $\mathbf{v}_k^c - \hat{\mathbf{v}}_k^c$. Figure 5.1(b) shows the results obtained. Here, accuracy is also improved until a polynomial of degree 5. Precision reduces from a polynomial of degree 6. Therefore, we take 5 as the optimal polynomial degree, since it assures a mean error of less than 0.1 pixels.

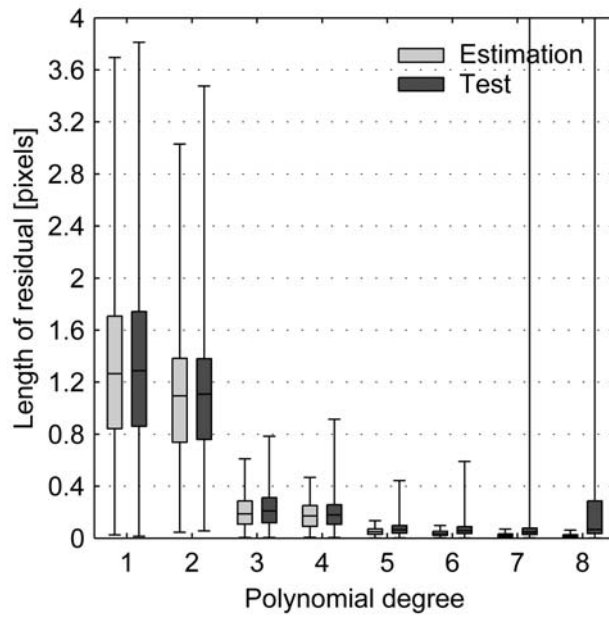
Note that in both cases the mean error on the calibration and the test set is very similar for polynomial 5. We explain it by the high number of calibration points used to estimate the polynomial. Note also that the error on the test set grows a lot for high polynomial degrees, whereas the calibration error remains small.

Although the two plots are very similar, they are not exact. This is due to the fact that, although being inverse transformations, the polynomial approximation can be of different complexities. In this case, though, the optimal polynomial degree is the same.

The obtained experimental results led us to conclude that the geometrical distortion introduced by the Image Intensifier can be accurately described by using a polynomial of degree 5. Thus, we can expect a mean error of less than 0.04 mm for a Field-Of-View of 17 cm when modelling the geometrical distortion using a polynomial of degree 5 for each view. Note that this choice also means that the optimal polynomial degree for the polynomials describing the steady component of distortion is 5.



(a)



(b)

Figure 5.1: Boxplot of the residual length for estimation and test points computed for different polynomial degrees. (a) for distortion polynomials $\rho_k^u(u, v)$ and $\rho_k^v(u, v)$, (b) for undistortion polynomials $\rho_k^{\hat{u}}(\hat{u}, \hat{v})$ and $\rho_k^{\hat{v}}(\hat{u}, \hat{v})$.

5.1.2 Focal Variation Influence

With this experiment, we aim to prove that varying the distance between the X-ray source and the Image Intensifier (i.e., the focal length f) does not affect the geometrical distortion. This is an important point, since the proposed model in section 3.1 uses only the orientation of the C-arm to estimate the distortion.

To assess the focal variation influence, we fixed a grid to the Image Intensifier screen. Then, we acquired a sequence of 124 frames while decreasing the focal distance f from 117cm to 87cm. For each frame k in the sequence, the crossing points $[\hat{\mathbf{u}}_k, \hat{\mathbf{v}}_k]$ were detected. As shown in figure 5.2, a change in the position of the crossing points can be noticed.

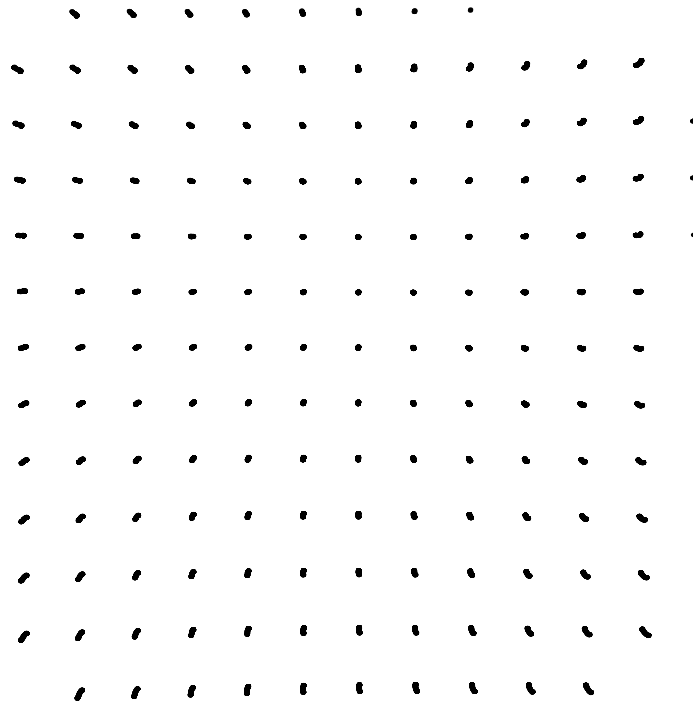


Figure 5.2: Evolution of the detected crossing points of a grid fixed to the Image Intensifier screen while varying the focal distance.

This change is mainly due to the fact that it is physically impossible to place the calibration grid on the image plane, but only slightly in front of the glass. Thus, a change in f results in a displacement of the crossing points. The question is whether a change in f invalidates the undistortion (and distortion) model.

To assess that, we performed the following experiment:

- First, we estimated for each frame of the sequence the ideal undistorted coor-

dinates $[\mathbf{u}_k, \mathbf{v}_k]$ of the detected crossing points $[\hat{\mathbf{u}}_k, \hat{\mathbf{v}}_k]$.

- Second, for the first image, we fitted the undistortion polynomials $\rho_0^{\hat{u}}(\hat{u}, \hat{v})$, $\rho_0^{\hat{v}}(\hat{u}, \hat{v})$ to $\mathbf{u}_0 - \hat{\mathbf{u}}_0$ and $\mathbf{v}_0 - \hat{\mathbf{v}}_0$, respectively.
- Finally, and for each frame k on the sequence and detected intersection point $(\hat{u}_{i,k}, \hat{v}_{i,k})$ with $i = 1 \dots N_k$, we computed the distance between ideal pixel coordinates $(u_{i,k}, v_{i,k})$ and the coordinates estimated using the distortion polynomials $\rho_0^{\hat{u}}(\hat{u}, \hat{v})$, $\rho_0^{\hat{v}}(\hat{u}, \hat{v})$ as follows:

$$E_{i,k} = \left\| [u_{i,k} - \hat{u}_{i,k} - \rho_0^{\hat{u}}(\hat{u}_{i,k}, \hat{v}_{i,k}), v_{i,k} - \hat{v}_{i,k} - \rho_0^{\hat{v}}(\hat{u}_{i,k}, \hat{v}_{i,k})] \right\|.$$

We followed a similar procedure for the distortion polynomials, and therefore computed the following error expression:

$$E_{i,k} = \left\| [\hat{u}_{i,k} - u_{i,k} - \rho_0^u(u_{i,k}, v_{i,k}), \hat{v}_{i,k} - v_{i,k} - \rho_0^v(u_{i,k}, v_{i,k})] \right\|,$$

where $\rho_0^u(u, v)$ and $\rho_0^v(u, v)$ were estimated using the first frame in the sequence.

The results obtained for all views are illustrated in figure 5.3: changing the focal distance does not affect the performance of neither the distortion nor the undistortion polynomials, since the error obtained is similar to the obtained in section 5.1.1. Thus, we conclude that a focal variation has a negligible effect on the geometrical distortion, and therefore it is not necessary to take it into account.

5.1.3 Optimal Polynomial Degree for $\delta_{\alpha,\beta}^u(u, v)$, $\delta_{\alpha,\beta}^v(u, v)$, $\delta_{\alpha,\beta}^{\hat{u}}(\hat{u}, \hat{v})$ and $\delta_{\alpha,\beta}^{\hat{v}}(\hat{u}, \hat{v})$

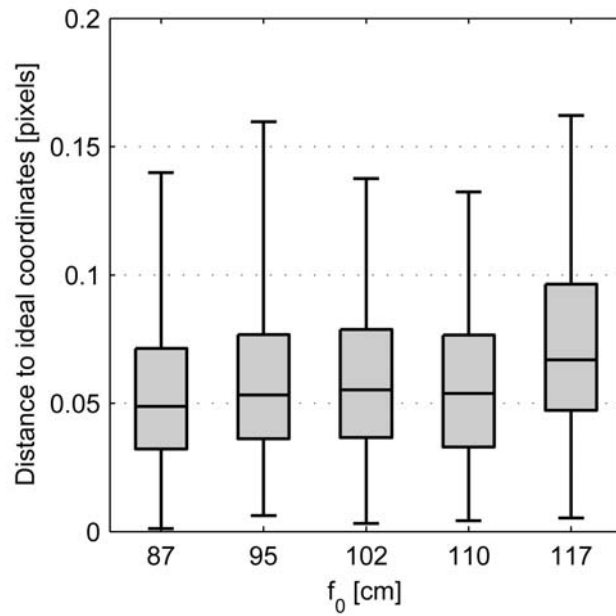
As stated in section 3.1, we decompose the distortion into two components, namely the steady and the orientation dependent one. We have already determined that the optimal polynomial degree for the steady component is 5. Therefore, in this experiment we aim determining the optimal polynomial degree of the polynomials modelling the orientation-dependent component. We expect obtaining a lower optimal polynomial degree for these polynomials, since this would justify the decomposition of the distortion polynomial into components $\bar{\rho}, \delta$.

To this aim, we acquired images of the grid fixed to the Image Intensifier screen considering 25 different orientations, namely for $\alpha = [-30, 0, 30, 60, 90]$ and $\beta = [20, 10, 0, -10, 20]$. For each view, we obtained about 150 crossing points and separated them in two sets: 50% of points to estimate the polynomials and the others to test the estimate obtained. Let $[\hat{\mathbf{u}}_k^c, \hat{\mathbf{v}}_k^c]$, $[\mathbf{u}_k^c, \mathbf{v}_k^c]$, be the distorted and undistorted coordinates of the crossing points in the calibration set for each view k . Analogously, for the test set we have $[\hat{\mathbf{u}}_k^t, \hat{\mathbf{v}}_k^t]$ and $[\mathbf{u}_k^t, \mathbf{v}_k^t]$.

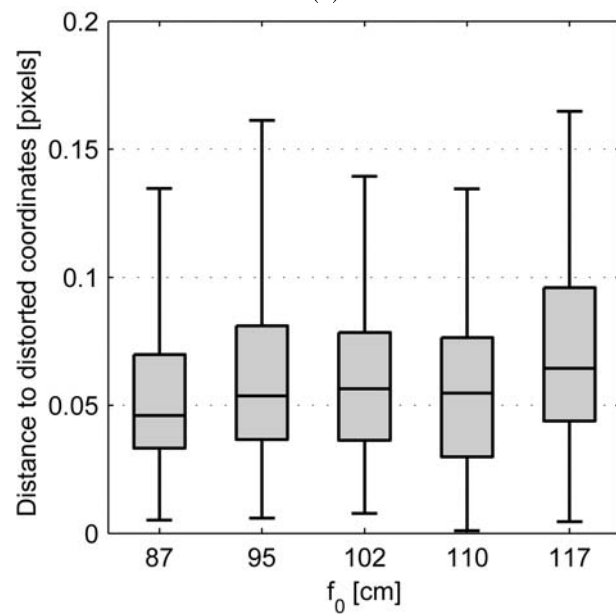
Using these data, we performed the following procedure:

- First, we estimated the coefficients of the polynomials modelling the steady component of distortion $\bar{\rho}^u(u, v)$, $\bar{\rho}^v(u, v)$ by fitting them to $\hat{\mathbf{u}}^c - \mathbf{u}^c$ and $\hat{\mathbf{v}}^c - \mathbf{v}^c$, respectively, where $\hat{\mathbf{u}}^c = [\mathbf{u}_0^c, \dots, \mathbf{u}_{24}^c]$ and $\hat{\mathbf{v}}^c = [\mathbf{v}_0^c, \dots, \mathbf{v}_{24}^c]$.

Hence, the distortion polynomials $\bar{\rho}^u(u, v)$, $\bar{\rho}^v(u, v)$ were fitted to all views and therefore the fitting error should correspond to the distortion variation due to the change in the orientation of the C-arm.



(a)



(b)

Figure 5.3: Boxplot of the error obtained, grouped for different values of focal length. (a) Focal variation influence on undistortion, (b) Focal variation influence on distortion.

- Then, for each view k , we computed the distortion variation surfaces $\Delta\rho_k^u, \Delta\rho_k^v$ as follows:

$$\begin{aligned}\Delta\rho_k^u &= \hat{\mathbf{u}}_k^c - \mathbf{u}_k^c - \bar{\rho}^u(\mathbf{u}_k^c, \mathbf{v}_k^c) \\ \Delta\rho_k^v &= \hat{\mathbf{v}}_k^c - \mathbf{v}_k^c - \bar{\rho}^v(\mathbf{u}_k^c, \mathbf{v}_k^c),\end{aligned}$$

In figure 5.4, we show the surfaces $\Delta\rho_k^u$ and $\Delta\rho_k^v$ of the fitting error as colormaps. The smoothness of obtained surfaces suggests that $\Delta\rho_k^u$ and $\Delta\rho_k^v$ can be approximated by low degree polynomials. Hence, the optimal polynomial degree for the distortion polynomials $\delta_{\alpha,\beta}^u(u, v)$ and $\delta_{\alpha,\beta}^v(u, v)$ is very likely to be low.

To confirm this hypothesis, for each view k we interpolated the surfaces $\Delta\rho_k^u$ and $\Delta\rho_k^v$ using the polynomials

$$\delta^u(u, v, \alpha_k, \beta_k) = \delta_k^u(u, v) \quad \text{and} \quad \delta^v(u, v, \alpha_k, \beta_k) = \delta_k^v(u, v),$$

respectively, where α_k and β_k are the rotation and angulation angles for view k .

The obtained results are presented in figure 5.5(a): from a polynomial of degree greater than 3, the fitting residual starts to grow. Similar results are obtained for the polynomials

$$\delta^{\hat{u}}(\hat{u}, \hat{v}, \alpha_k, \beta_k) = \delta_k^{\hat{u}}(\hat{u}, \hat{v}) \quad \text{and} \quad \delta^{\hat{v}}(\hat{u}, \hat{v}, \alpha_k, \beta_k) = \delta_k^{\hat{v}}(\hat{u}, \hat{v}),$$

which interpolate

$$\begin{aligned}\Delta\rho_k^{\hat{u}} &= \mathbf{u}_k^c - \hat{\mathbf{u}}_k^c - \bar{\rho}^{\hat{u}}(\hat{\mathbf{u}}_k^c, \hat{\mathbf{v}}_k^c) \\ \Delta\rho_k^{\hat{v}} &= \mathbf{v}_k^c - \hat{\mathbf{v}}_k^c - \bar{\rho}^{\hat{v}}(\hat{\mathbf{u}}_k^c, \hat{\mathbf{v}}_k^c)\end{aligned}$$

where $\rho^{\hat{u}}(\hat{u}, \hat{v})$ and $\rho^{\hat{v}}(\hat{u}, \hat{v})$ were fitted to $\mathbf{u}^c - \hat{\mathbf{u}}^c$ and $\mathbf{v}^c - \hat{\mathbf{v}}^c$, respectively.

The obtained results are shown in figure 5.5(b).

From this experiment, we can conclude that the choice of a polynomial of degree 3 for the polynomials $\delta_{\alpha,\beta}^u(u, v)$ and $\delta_{\alpha,\beta}^v(u, v)$ leads to a mean error of less than 0.1 pixels for both distortion models, that corresponds to less than 0.04mm for a FOV of 17cm. The same conclusion can be derived for the polynomials $\delta_{\alpha,\beta}^{\hat{u}}(\hat{u}, \hat{v})$ and $\delta_{\alpha,\beta}^{\hat{v}}(\hat{u}, \hat{v})$.

Note that this result is very similar to the accuracy obtained in the experiment from section 5.1.1, where a different 5th degree polynomial was fitted for each view. Here we fit unique 5th degree polynomial $\bar{\rho}$ for all views, and a polynomial δ_k of only 3th degree for each view k . Therefore, using less polynomial coefficients we obtain similar accuracy results, and hence the decomposition of the distortion into two components is justified.

5.1.4 Determination of the Optimal Polynomial Degree for $\{\omega^{u,i}(\alpha, \beta)\}$, $\{\omega^{v,i}(\alpha, \beta)\}$, $\{\omega^{\hat{u},i}(\alpha, \beta)\}$, and $\{\omega^{\hat{v},i}(\alpha, \beta)\}$

We illustrated that the geometrical distortion is only affected by the orientation of the C-arm and by the spatial distribution of pixels in the image plane. Hence, the coefficients of the polynomials that model the orientation-dependent component

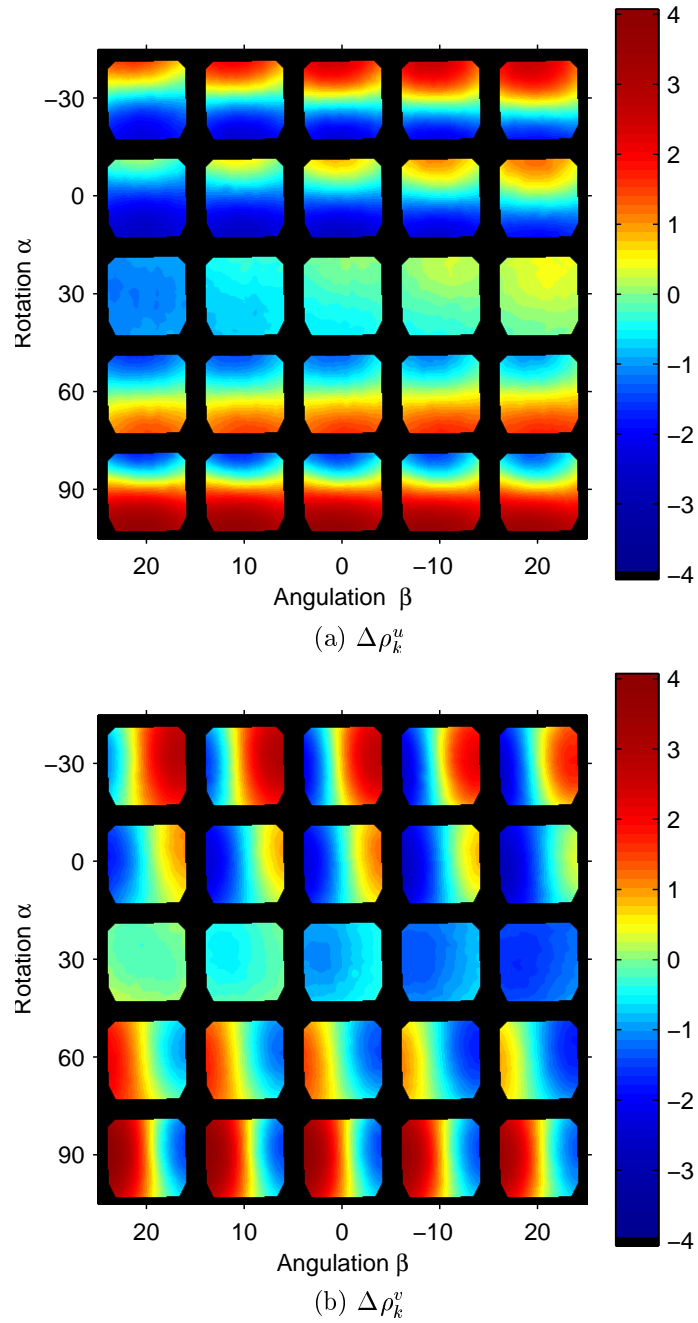
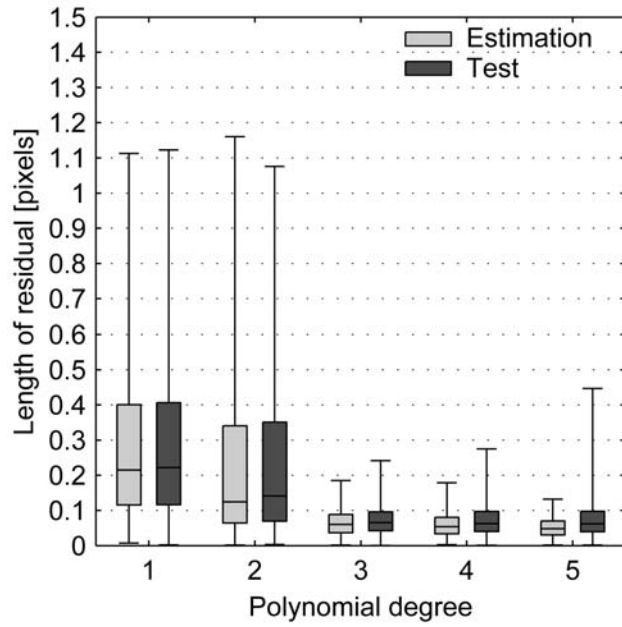
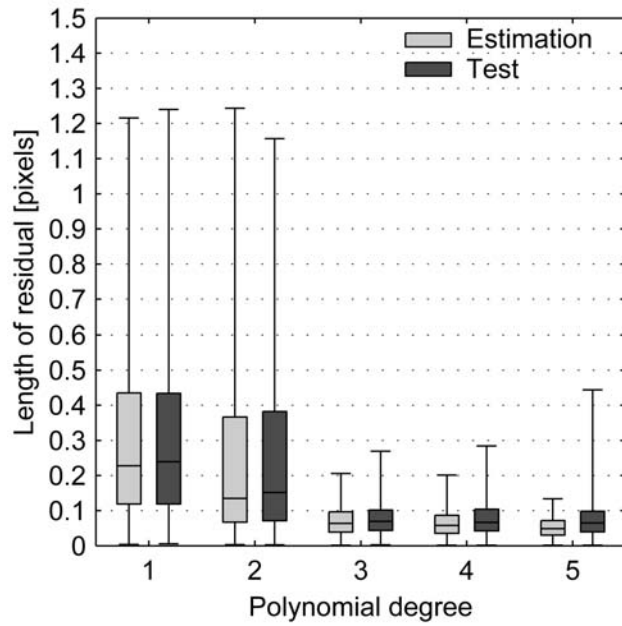


Figure 5.4: Color-map displaying the distortion variation as the anatomical angles α and β vary. $\Delta\rho_k^u$ and $\Delta\rho_k^v$ are both in pixels.



(a)



(b)

Figure 5.5: Boxplot of the residual length for estimation and test points. (a) For different polynomial degrees of $\delta_k^u(u, v)$ and $\delta_k^v(u, v)$; (b) for different polynomial degrees of $\delta_k^u(\hat{u}, \hat{v})$ and $\delta_k^v(\hat{u}, \hat{v})$.

of the distortion (namely, $\delta_{\alpha,\beta}^u(u, v)$, $\delta_{\alpha,\beta}^v(u, v)$, $\delta_{\alpha,\beta}^{\hat{u}}(\hat{u}, \hat{v})$ and $\delta_{\alpha,\beta}^{\hat{v}}(\hat{u}, \hat{v})$) should be estimable by means of a function of the parameters α and β , which are clearly related to the orientation of the detector. The aim of this experiment is to prove that this function can be a bi-variate polynomial of α and β , as proposed in section 3.1, and to determine the optimal polynomial degree to obtain the better estimation results.

To this aim, we used the previous acquisitions at $\alpha = [-30, 0, 30, 60, 90]$ and $\beta = [20, 10, 0, -10, -20]$ as the estimation set for this experiment. For the test set we acquired views at $\alpha = [-15, 15, 70]$ and $\beta = [15, 5, -5, -15]$. For each view k on the estimation set, we estimated the polynomials $\delta_k^u(u, v)$, $\delta_k^v(u, v)$, $\delta_k^{\hat{u}}(\hat{u}, \hat{v})$ and $\delta_k^{\hat{v}}(\hat{u}, \hat{v})$ (see the previous experiment for details).

From this data, we performed the following:

- First, for each coefficient in the polynomials δ_k , we fitted the corresponding polynomial ω . For instance, the j th coefficient of $\delta_k^u(u, v)$ was interpolated using the polynomial $\omega^{u,j}(\alpha, \beta)$ for different polynomial degrees, which has the following expression:

$$\omega^{u,j}(\alpha_k, \beta_k) = \sum_{n=0}^N \sum_{m=0}^n d_i^{u,j} \alpha_k^{n-m} \beta_k^m$$

where $i = \frac{n(n+1)}{2} + m$ and N is the polynomial degree. Hence, its coefficients $\{d_i^{u,j}\}$ were chosen to minimize the following:

$$\sum_{k=0}^K (c_j^{u,k} - \omega^{u,j}(\alpha_k, \beta_k))^2$$

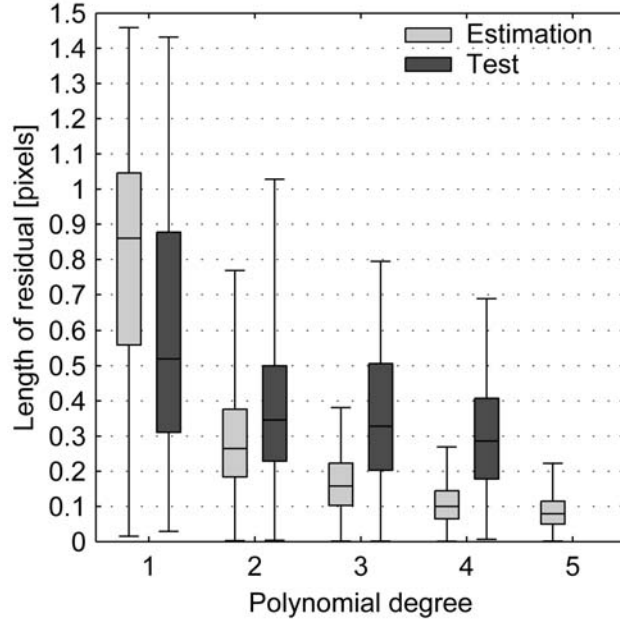
where $c_j^{u,k}$ is the j th coefficient of $\delta_k^u(u, v)$ and α_k, β_k the rotation and the angulation angles for view k . To simplify the experiment, we constrained all the coefficients to be estimated with a same polynomial degree N . For details on bi-variate polynomial fitting, see Appendix C.

- Second, the obtained polynomials $\{\omega^{u,j}(\alpha, \beta)\}$, $\{\omega^{v,j}(\alpha, \beta)\}$, $\{\omega^{\hat{u},j}(\alpha, \beta)\}$ and $\{\omega^{\hat{v},j}(\alpha, \beta)\}$ were used to compute the polynomials $\delta^u(u, v, \alpha, \beta)$, $\delta^v(u, v, \alpha, \beta)$, $\delta^{\hat{u}}(\hat{u}, \hat{v}, \alpha, \beta)$ and $\delta^{\hat{v}}(\hat{u}, \hat{v}, \alpha, \beta)$, respectively. For instance, we computed the polynomial $\delta^u(u, v, \alpha, \beta)$ as:

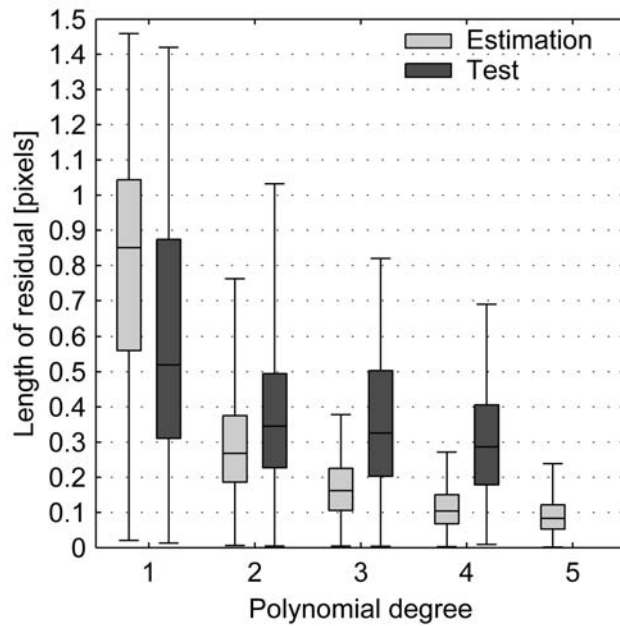
$$\delta^u(u, v, \alpha, \beta) = \delta_{\alpha,\beta}^u(u, v) = \sum_{n=0}^3 \sum_{m=0}^n \omega^{u,j}(\alpha, \beta) u^{n-m} v^m$$

where $j = \frac{n(n+1)}{2} + m$. Note that we have used 3 as polynomial degree for $\delta_{\alpha,\beta}^u(u, v)$, as estimated in the previous experiment.

Then, we evaluated the performance of the obtained polynomials to model the distortion, for each view set and polynomial degree N . The results obtained are shown in figure 5.6.



(a)



(b)

Figure 5.6: Boxplot of the residual length for estimation and test views. (a) Distortion model for different polynomial degrees of $\{\omega^{u,i}(\alpha, \beta)\}$ and $\{\omega^{v,i}(\alpha, \beta)\}$. (b) Undistortion model for different polynomial degrees of $\{\omega^{u,i}(\alpha, \beta)\}$, and $\{\omega^{v,i}(\alpha, \beta)\}$. The error for the test data and polynomial degree of 5 is so big (more than 10 pixel) that it does not appear in this plot.

For a polynomial of degree greater than 4, the error rapidly increases. This is caused by the low number of calibration views. For a polynomial of degree $N=5$, we need at least $\frac{(N+2)(N+1)}{2} = 21$ views for exact data. Since we have used only 25 views, that is, only 3 views more, it is hard to overcome the noise. We expect that by increasing the number of views, the error should decrease. Anyway, with only 25 calibration acquisitions and a polynomial of degree 4, we can expect a mean error below 0.3 pixels for both distortion and undistortion models, which equals to 0.1mm for a FOV of 17cm.

Note that the obtained error is bigger compared to the obtained in the previous experiments. The reason is that now we have a global model of distortion. However, the obtained accuracy is still quite acceptable, and hence we conclude that using this model, we can accurately correct the distortion without the need of calibrating distortion at each acquisition. This fact greatly simplifies the clinical application of three-dimensional reconstruction techniques.

5.2 Model for the Acquisition Geometry

The main objective of the following experiments is to evaluate the performance of the different proposals regarding the determination of the acquisition geometry, which were presented in section 3.2. Hence, our first experiment aims to determine whether the calibration method proposed by Zhang in [103] is applicable to the angiographic frame. After validating this issue, the calibration obtained serves as input data to the next experiment, in which we evaluate each of the models proposed in section 3.2 using a cross-validation scheme.

As stated before, we are performing our experiments with a SIEMENS Cathcor 3.3 C-arm angiography acquisition system in the University Hospital "Germans Trias i Pujol" (Badalona, Spain). This system is laterally mounted instead of ceiling-mounted. Figure 5.7 illustrates how anatomical angles are defined in our system.

This situation is different from the considered in the paper of Dumay et al. [22], and therefore different from that of section 3.2. To solve this problem, we must replace α by $-\alpha$ and β by $-\beta$ before performing the experiments.

5.2.1 Zhang's Calibration on a SIEMENS C-Arm

To evaluate whether the calibration method proposed by Zhang in [103] is applicable in the angiographic frame, we acquired the grid for different positions of the C-arm, namely for $\alpha \in \{-30, -15, -5, 0, 5, 15, 30\}$ and $\beta \in \{-20, -15, -10, 0, 10, 15, 20\}$. Then, we carried out the following:

- First, for each view i we detected the M grid nodes, obtaining $\hat{\mathbf{u}}_i = [\hat{u}_{i1}, \dots, \hat{u}_{iM}]$ and $\hat{\mathbf{v}}_i = [\hat{v}_{i1}, \dots, \hat{v}_{iM}]$. The real positions of the grid nodes in world coordinates were also obtained, which are denoted as $\mathbf{x} = [x_1, \dots, x_M]$, $\mathbf{y} = [y_1, \dots, y_M]$.
- Second, we applied the undistortion model calibrated in section 5.1 to obtain the undistorted coordinates $\mathbf{u}_i = [u_{i1}, \dots, u_{iM}]$, $\mathbf{v}_i = [v_{i1}, \dots, v_{iM}]$.

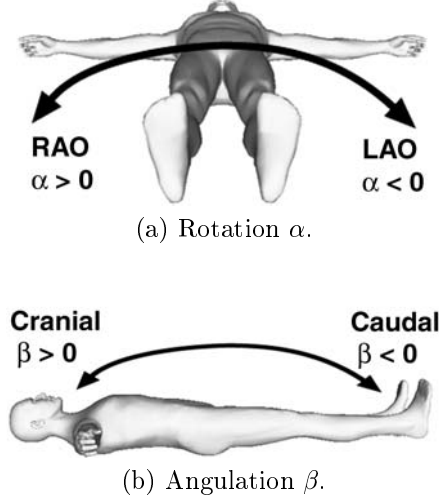


Figure 5.7: Anatomic angles for a laterally mounted SIEMENS Cathcor 3.3 C-arm, which define the orientation of the detector.

- Third, we obtained an estimation of \mathbf{A} , $\{\hat{\mathbf{R}}_i\}$ and $\{\hat{\mathbf{t}}_i\}$. To do that, we followed Zhang’s calibration method[103] using the undistorted crossing points $\mathbf{u}_i, \mathbf{v}_i$ on each view i and the corresponding real world coordinates \mathbf{x}, \mathbf{y} .
- Finally, we used the following expression to evaluate the calibration error:

$$E_{ij} = \left\| \begin{bmatrix} u_{ij} \\ v_{ij} \end{bmatrix} - \mathbf{A}[\hat{\mathbf{R}}_i - \hat{\mathbf{t}}_i] \begin{bmatrix} x_{ij} \\ y_{ij} \\ \mathbf{0} \\ \mathbf{1} \end{bmatrix} \right\|$$

for each view i and grid node j .

The standard deviation of the obtained $\{E_{ij}\}$ was of 0.13 pixels, and the maximum value 0.8 pixels. Therefore, if we project the grid nodes using the estimated \mathbf{A} , $\{\hat{\mathbf{R}}_i\}$ and $\{\hat{\mathbf{t}}_i\}$, the positions obtained will be pretty near to the real ones. Hence, we conclude that Zhang’s calibration model is also applicable in the angiographic frame.

5.2.2 Accuracy Evaluation for M0, M1, M2, M3 and M4

The aim of this experiment is to determine which model fits best to the real movement of the C-arm. To this aim, we did the following:

- First, we randomly divided the estimated $\hat{\mathbf{R}}_i$ and $\hat{\mathbf{t}}_i$ of the previous experiment in two sets: the calibration and the test set.
- Using the rotation and translation matrices of the calibration set, we estimated the parameters of each of the models **M0**, **M1**, **M2**, **M3** and **M4**, following the method described in section 3.2.3.

- Finally, we evaluated the accuracy obtained for each model. To this aim, we have evaluated the following expression for each view i and position j :

$$E_{ij}^k = \left\| \begin{bmatrix} u_{ij} \\ v_{ij} \end{bmatrix} - \mathbf{A}[\mathbf{R}_i^k \mathbf{t}_i^k] \begin{bmatrix} x_{ij} \\ y_{ij} \\ \mathbf{0} \\ \mathbf{1} \end{bmatrix} \right\|$$

where matrices \mathbf{R}_i^k and \mathbf{t}_i^k are the predicted extrinsic parameters for view i and model \mathbf{M}_k , using the estimated parameters.

Table 5.2.2 shows the results obtained. From these results, we can state that the

	Calibration		Test	
	std($\ E\ $)	max $\ E\ $	std($\ E\ $)	max $\ E\ $
M0	6.81	33.38	5.63	23.00
M1	1.80	10.15	1.85	9.77
M2	1.98	13.14	1.96	11.07
M3	1.08	8.49	1.00	4.77
M4	0.91	5.39	0.86	5.44

Table 5.1: Displacement E (in pixels) between the detected intersection points on the grid and predicted positions for each model, computed both for calibration and test sets.

models which better fit are **M3** and **M4**. Note the large maximal errors introduced by model **M0**. Since the distance between wires on the grid is of 1cm and the projected gap on the image measures a mean of 40 pixels, an error of 30 pixels is very important.

Hence, we can conclude that the assumptions made by the model of Dumay et al. in [22] to define model **M0** are not fulfilled in the angiographic system where we have performed our tests. In particular, the assumptions of image alignment, isocenter existence and perfect orthogonality between the angulation and rotation axis should not be done for this case. Hence, in order to model the movement of the C-arm, we conclude that the proposed models **M3** and **M4** are in this case much more appropriate than the classical isocentric model **M0**.

5.3 Biplane Snakes

To discuss the practical issues of the proposed biplane snakes for the three-dimensional reconstruction, we carried out experiments with synthetic images, real images of a phantom, and real cardiac images.

Second, we use real X-ray images of wire phantoms to evaluate the three-dimensional reconstruction accuracy using the model **M4**, and to discuss some practical cases with long complex shapes and vessel overlaps.

Finally, we show some examples of the three-dimensional reconstruction of coronary vessels on real cardiac images.

5.3.1 Experiments with Synthetic Images

The following experiments were all performed on synthetically generated images. First, we compare the obtained three-dimensional reconstruction accuracy using biplane snakes to the obtained with manual reconstruction. Second, we study the biplane snakes performance when approaching the reconstruction of wavy vessels. Finally, we evaluate the influence of image distortion on the 3D reconstruction accuracy.

Manual Reconstruction vs. Biplane Snakes

This experiment compares the performance of biplane snakes to the manual reconstruction. To this aim, we defined 5 different curves and generated two simulated views for each one. Then, four experts (*obs1*, *obs2*, *obs3*, *obs4*) were asked to mark corresponding points of the curve as exactly as possible in order to achieve a manual reconstruction. The epipolar line helped the users to determine point correspondences, and the users were allowed to modify the control points to improve the accuracy. We also obtained a three-dimensional reconstruction using biplane snakes for each image pair. The curve generated by each user was then used as initial shape for the snake, which was allowed to deform up to 500 iterations. Figure 5.8(a) shows the results obtained. The mean relative improvement of error was of 9% when using biplane snakes.

We repeated the experiment, but now introducing random error in the intrinsic and extrinsic parameters used to obtain the three-dimensional reconstruction. The obtained results are shown in figure 5.8(b). This time, the main relative improvement error using biplane snakes was of 12%.

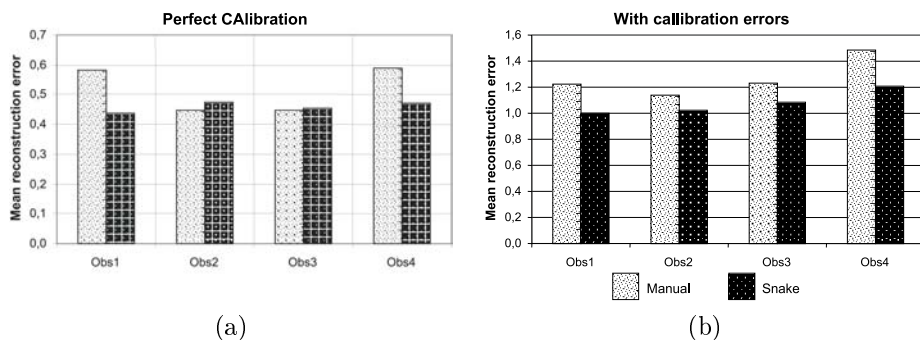


Figure 5.8: Mean reconstruction error for computational phantom.

From these results, we can derive two conclusions: First, when the acquisition conditions are known with high precision, biplane snakes obtain a three-dimensional reconstruction as good as the obtained using manual reconstruction. Second, with noise on the estimation of the acquisition conditions, biplane snakes obtain a more accurate three-dimensional reconstruction.

Biplane Snakes Behaviour against Wavy Vessels

This experiment compares the performance of biplane snakes using distance map gradient as external force to the performance of their extension using the Generalized Gradient Vector Flow (GGVF).

To this aim, we constructed a synthetic phantom of a wavy vessel by sampling the 3D curve:

$$p(s) = (5s, 3 \cos(9s) \sin(6s), 3 \sin(9s) \cos(6s))$$

at $s \in [-0.5, 0.5]$ with step 10^{-3} . Then, for 10 different views, we proceeded as follows: First, we applied the corresponding projection matrix to the sampled curve to obtain the projection of the curve in undistorted pixel coordinates. From these coordinates, we constructed a 512×512 image matrix ¹, which was directly used to compute the distance map and the GGVF.

Then, and for each image pair, we proceeded as follows:

- First, we initialized both snakes exactly with the same shape. Figure 5.9(a) shows the initial position of the snake for one of these image pairs. The first image view simulates an acquisition for $\alpha = 0$, $\beta = 0$ and $f = 95\text{cm}$. The second image view is defined by parameters $\alpha = -30$, $\beta = -20$ and $f = 95\text{cm}$.
- Then, we deformed both snakes until the change of the positions of the control points was less than 0.1 pixel. The stiffness of both snakes was controlled with elastic parameters (membrane parameter 0.1 and thin-plate parameter 0.01). Figure 5.9(b) shows the final position of the Distance Map (DM)-based snake and figure 5.9(c) corresponds to the final position for the GGVF-based snake.
- Once the snake converged, we estimated the mean error by computing the distance from each point on the sampled 3D snake to the corresponding nearest sampled point on the sampled 3D curve phantom.

As expected, the DM-based snake cannot deal with concave shapes and results in a mean three-dimensional error of 4.26mm, and a maximum of 11.56mm, since the snake has not converged to the concave location of the vessel². On the other hand, the snake with external energy based on GGVF obtains a mean three-dimensional error of 0.18mm and a maximum error of 0.89mm. The maximum error corresponds to the points of maximum concavity.

From these results we conclude that the Distance Map is not a good choice when reconstructing wavy vessels. Instead, it is better to use the GGVF as external force of the snake.

Influence of Image Distortion

In this experiment we follow the same procedure to obtain the views of the synthetic phantom, but now we apply the distortion model estimated in section 5.1.4 to

¹We generated a curve, representing the "vessel" centerline. The analysis of the performance of vessel centerline algorithms is out of the scope of this thesis.

²The actual length of the simulated curve is of 224.5mm

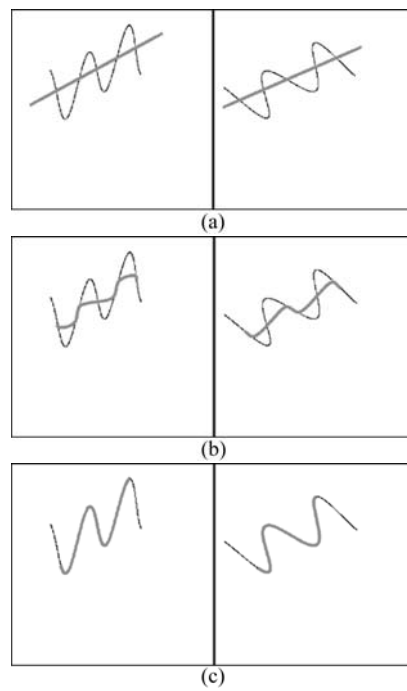


Figure 5.9: Capture performance of concave shapes for both kinds of snakes. View 1 (left) is simulated for $\alpha = 0$, $\beta = 0$ and $f = 95\text{cm}$ and view 2 (right) for $\alpha = -30$, $\beta = -20$ and $f = 95\text{cm}$; (a) shows the initial position for both snakes, (b) the final position for the (DM)-based snake, and (c) the final position for the GGVF-based snake.

the projected coordinates of the phantom before constructing the image. Thus, in this case we obtain a distorted simulated view. As before, we generated 10 different views, and computed the GGVF for each view. For each image pair, we deformed a GGVF-based snake until convergence, and a GGVF-based snake considering distortion.

The projected final position of the GGVF-snake for the previous view pair (which is now distorted) is presented in figure 5.10(a). Figure 5.10(b) shows that the snake clearly differs on the 3D space from the phantom.

When distortion is not taken into account, the obtained mean error for a GGVF-based snake is 1.40mm, with a maximum of 2.64mm. On the other hand, by considering distortion the obtained mean error for a GGVF-based snake is 0.17mm, with a maximum of 0.87mm. This maximum is placed again at concavities.

From this results, we conclude that taking into account distortion really improves the three-dimensional reconstruction accuracy. In particular, the mean error reduction is near the 80%.

5.3.2 Tests on Real Images

In the following experiments the extreme points of the snake are not modified during the deformation. That is the way we proceed in the actual applications of the technique (i.e. lesion measurement and catheter path reconstruction for IVUS and X-ray data fusion purposes). The deformation was performed in two steps: first we deformed the snake with elastic parameters $\alpha = 0.0$ and $\beta = 0.1$, and then we refined the snake by decreasing its stiffness using a thin-plate parameter of 0.01 in order to capture the details.

All the following experiments were performed using real images, acquired at the Hospital Universitari "Germans Trias i Pujol".

3D Reconstruction of a Wire Phantom

This experiment was designed to see the accuracy obtained when reconstructing a curvilinear phantom using biplane snakes. Also, the different proposed models **M0**, **M1**, **M2**, **M3** and **M4** are evaluated.

Three months after the calibration date, we have acquired a phantom simulating a vessel, and consisting on a wavy wire. The wire was imaged for different views, namely, for $\alpha \in [30^\circ, 0^\circ, -30^\circ]$ and $\beta \in [15^\circ, 0^\circ, -15^\circ]$.

We have then estimated for each model **M0**, **M1**, **M2**, **M3** and **M4** the corresponding extrinsic parameters for all views by using the parameters obtained in section 5.2.2.

For each model **M0**, **M1**, **M2**, **M3** and **M4**, we have reconstructed the phantom using a biplane snake (for a description of biplane snakes, see [8]) and views $[\alpha_1 = 30^\circ, \beta_1 = 0^\circ]$ and $[\alpha_2 = -30^\circ, \beta_2 = 0^\circ]$. We have done two reconstructions: ignoring the distortion introduced by the Image Intensifier, and using the distortion/undistortion model estimated in section 5.1. Figure 5.11 shows the obtained three-dimensional shape and the reconstruction views.

Finally, we have projected the reconstructed curve on the other views, to see

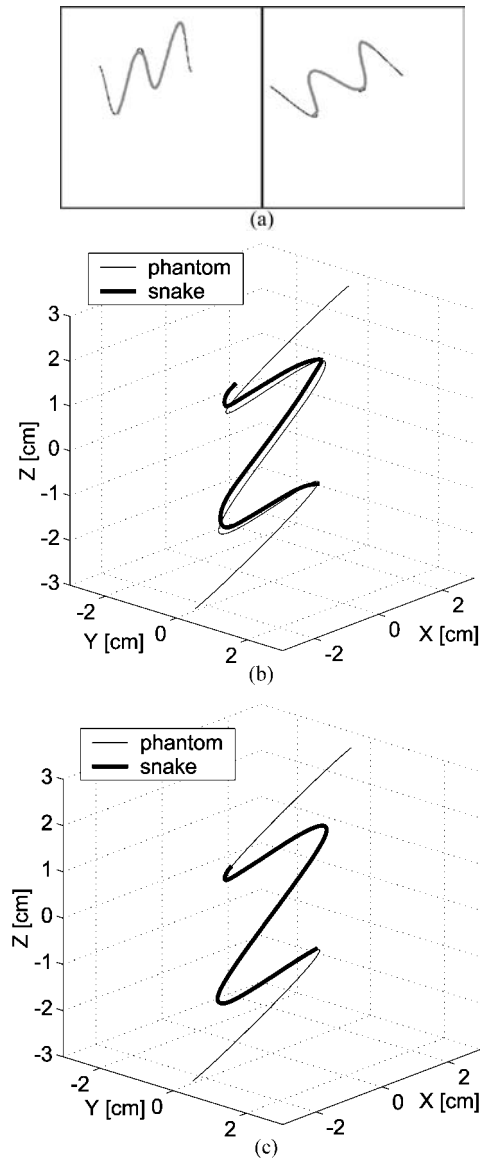


Figure 5.10: Distortion influence on reconstructing a 3D concave shape. Part (a) shows the final projected position for (GGVF)-based snake. View 1 (left) is simulated for $\alpha = 0, \beta = 0$ and $f = 95\text{cm}$ and view 2 (right) for $\alpha = -30, \beta = -20$ and $f = 95\text{cm}$. Each view is distorted using the distortion model estimated in section 5.1.4. Part (b) is the final 3D position for (GGVF)-based snake without considering distortion and (c) by considering distortion.

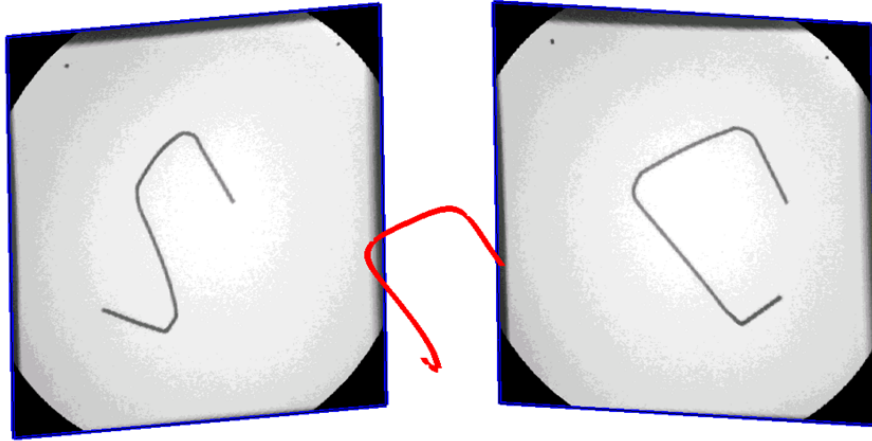


Figure 5.11: 3D reconstruction of a wire phantom from two views.

whether the projection of the curve fits the image. Figure 5.3.2 shows the obtained curve projected for a view with $\alpha = 0$ and $\beta = 15$, for each model. Note that the curve fits pretty accurately for models **M3** and **M4**. Numerical results are presented in table 5.2.

Model	Ignoring distortion		Including distortion	
	\bar{D}_i	$\max \bar{D}_i$	\bar{D}_i	$\max \bar{D}_i$
M0	4.0	7.9	3.4	7.5
M1	0.6	1.5	0.6	1.4
M2	0.5	1.5	0.5	1.4
M3	0.4	0.9	0.2	0.5
M4	0.3	0.6	0.1	0.3

Table 5.2: Here D is the distance from each projected point of the curve to the nearest position on the image corresponding to wire. \bar{D}_i is the mean of distance D for all views, and $\max \bar{D}_i$ is the maximum value of the mean distance computed for each view. All values are in pixels.

From these results, we can conclude that the biplane snakes can accurately reconstruct a curvilinear shape, provided that they use the models **M3** or **M4** for the extrinsic parameters. The influence of image distortion is less perceptible, although it has also some influence.

Note that these accuracy results are much better than the obtained when testing the accuracy using a grid and corresponding points. The reason of this is that here we compare the distance of each point of the projected curve to the nearest point corresponding to the wire, and this distance is minimized by biplane snakes.

The calibration was performed three-months before the reconstruction date, and the accuracy results are still quite acceptable. This fact encourages us to state that

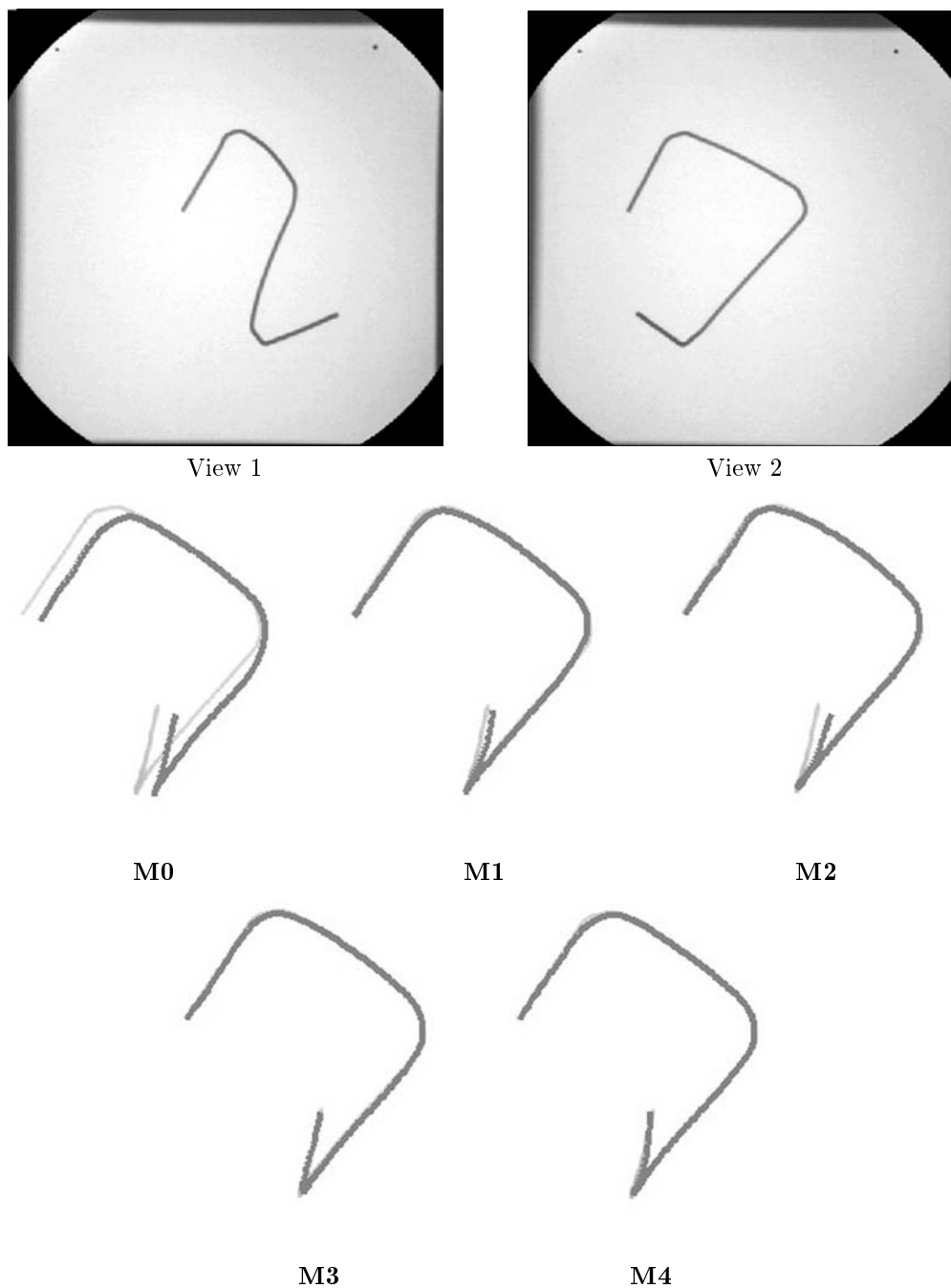


Figure 5.12: Projection of the reconstructed 3D curve (dark) using each model at $\alpha = 0, \beta = 15$. The curve was obtained from views $\alpha = 30, \beta = 0$ (view 1) and $\alpha = -30, \beta = 0$ (view 2). Geometrical distortion introduced by the Image Intensifier was taken into account.

by using models **M3** or **M4**, it shall not be necessary a calibration nor a refinement at each acquisition, as proposed in [23, 13, 28], but only a periodic calibration. This fact is very important, since it highly simplifies the clinical application of diagnostic techniques involving 3D reconstruction from angiographies.

Behaviour of Biplane Snakes

After assessing the accuracy of the three-dimensional reconstruction, we studied the different problems that could appear in practice when using biplane snakes.

To this aim, we performed several tests on a phantom made of plastic which could be injected with contrast. Figures 5.13(a) and 5.13(b) show the phantom acquired from two different views and the extracted features. Figures 5.13(c) and 5.13(d) show one of the tested initializations of the snake and the corresponding projected GGVF snake evolution. Note that the snake overcomes the potential problems with missing features due to occlusions and converges to the target vessel despite the poor initialization.

Whereas this kind of phantom is a good approximation to a real vessel, it has the drawback that its shape is very simple. Therefore, we also used 5 segments of wire with various shapes to test biplane snakes. In most cases, the snake correctly converged to the target shape without difficulties and with only two initialization points.

A more complex situation occurs when the wire is overlapped by other vessels, overlaps itself or the desired deformation path is intersected by other objects. That is the case of figures 5.14(a) and 5.14(b), where the snake could not converge to the correct position (the snake evolution is plotted in black and the initialization in white).

In these cases, an easy solution is to increase the number of initialization points, as shown in figures 5.14(c) and 5.14(d), where two extra initialization points were added. Note that a great accuracy is not necessary when marking the extra points. Figures 5.14(e) and 5.14(f) show the snake evolution (in black) from the new initial position (in white). Alternatively, the user can also interact with the snake to guide its deformation, but this was not necessary in any of the performed tests.

Hence, we can conclude that biplane snakes overcome the problems introduced by missing features on the image, as other deformable models do. Moreover, when facing up long complex shapes, overlapped vessels or others ambiguities, the user can easily overcome these situations by introducing some extra initialization points. However, in most cases the shape to be reconstructed will be very simple and therefore only two initialization points will be necessary.

Examples on Real Cardiac Images

Here we show some examples of the three dimensional reconstruction of vessels from real cardiac images. Since the angiographic system present at Hospital Universitari "Germans Trias i Pujol" is a monoplane system, the patients were asked to exhale all the air before contrast injection and to suspend the breathing during the acquisition. Also, special care was taken to avoid changes on the position of the patient between acquisitions. The frames to be reconstructed were selected to be at

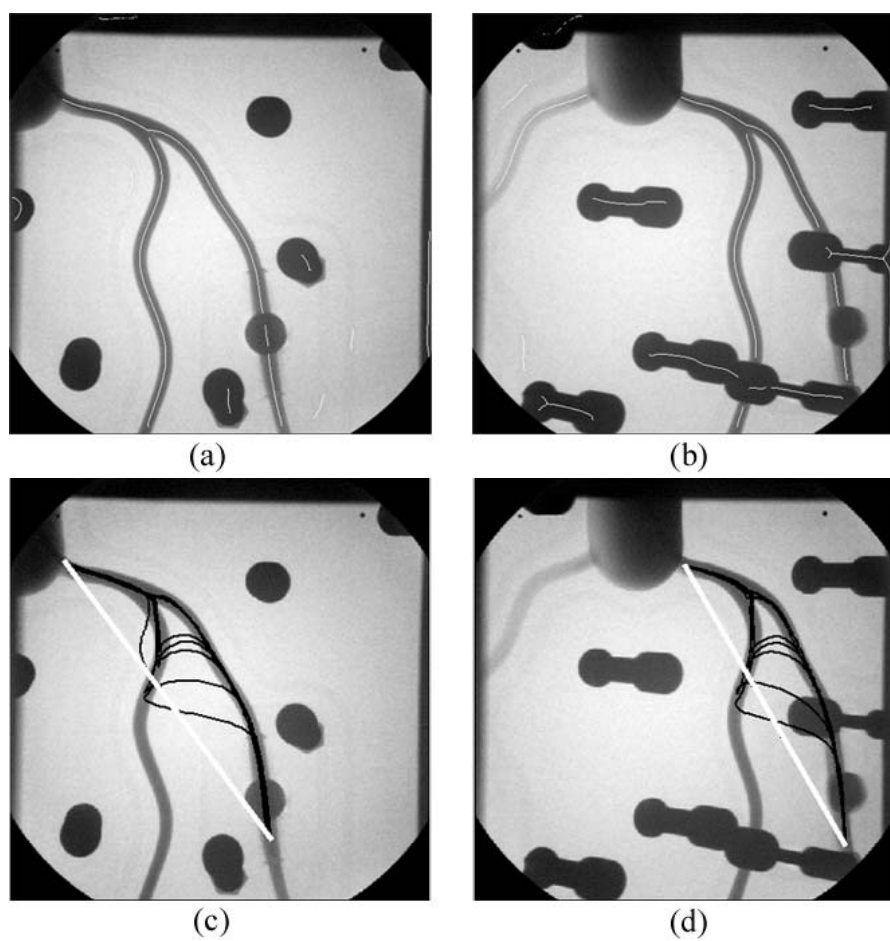


Figure 5.13: 3D reconstruction of a phantom with contrast from two views. (a) and (b) show the detected features and (c) and (d) the projected initial position of the snake (in white) and the snake evolution (in black).

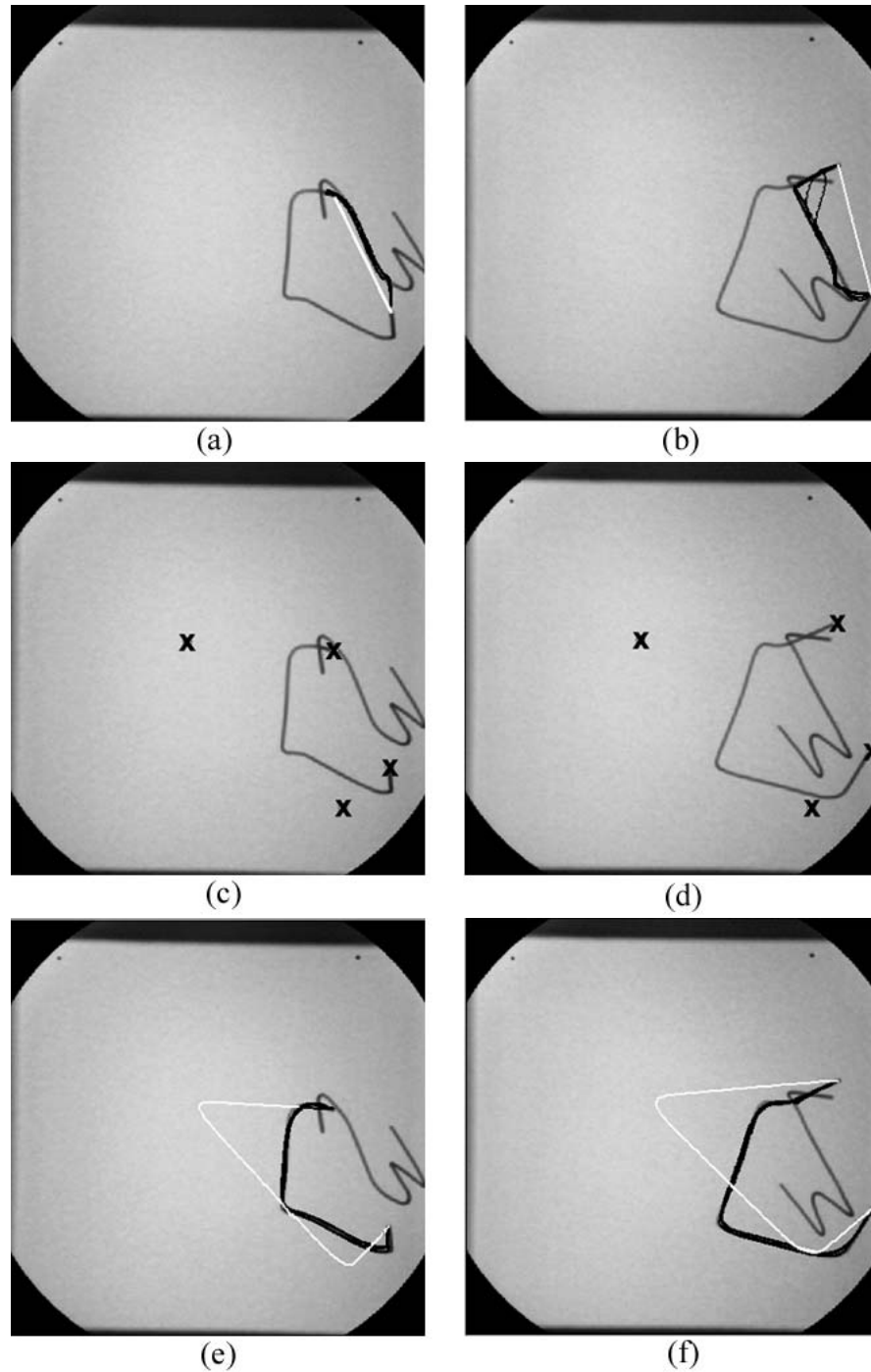


Figure 5.14: 3D reconstruction of two wires. (a) and (b) show the deformation of the snake (in black) from the initial shape (in white). The final shape is incorrect, since the snake has been confused by the other wire. As a solution, the user can introduce two extra initialization points, as shown in (c) and (d). Using this points, the snake can reach the correct position, as show in (e) and (f).

the end of diastole using the ECG.

Figure 5.15 show the result of the feature extraction method proposed in [51] on two cardiac images from two patients. Any other vessel-centerline extraction method is applicable here, as the ones described in [37].

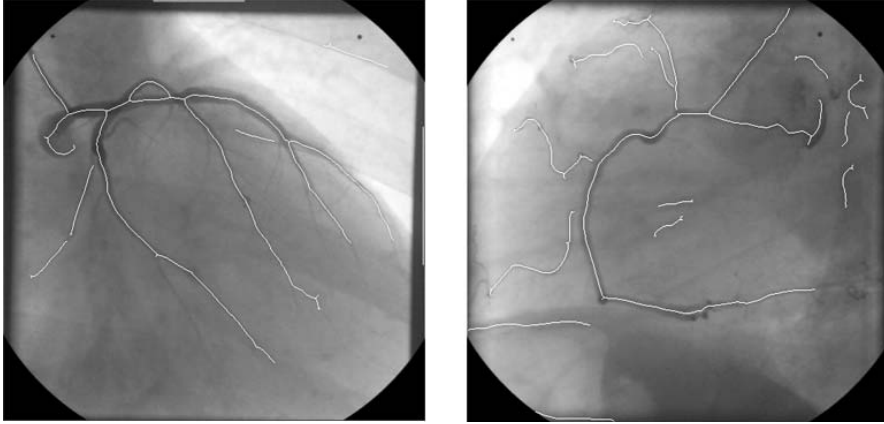


Figure 5.15: Vessel centerline features, which are used to compute the GGVF that guides the deformation of the snake.

We performed tests on 5 patients. For each patient, we acquired three projections of the heart. The first two were used to reconstruct and the third to test the reconstruction obtained by projecting the final snake onto it.

Figures 5.16(a) and 5.16(b) are two projection pairs used to reconstruct a vessel segment. Figure 5.16(c) shows the projection on a third view of the obtained 3D curve from the first pair, and figure 5.16(d) the projection of the curve from the second pair. Note that both projected curves coincide with the vessel appearance in the image. We used between 1 and 3 extra initialization points to reconstruct the vessel segments. However, for many applications, as lesion measurement, we will be interested in much smaller vessel segments, and therefore in most cases only two initialization points will be required.

5.4 Vessel Enhancement Diffusion

The experiments presented in this section were designed to evaluate the performance of the Vesselness Enhancement Diffusion filter. To this aim, we compare three different approaches to detect the vessels using Frangi's vesselness measure: with no extra pre-processing, by applying Solé's filter [85] before computing the vesselness, and using our Vesselness Enhancement Diffusion filter, which is proposed in section 4.2.1.

We quantitatively evaluated the performance of each of these approaches using synthetic images. Afterwards, we tested the three approaches on real cardiac images for a qualitative evaluation of the methods.

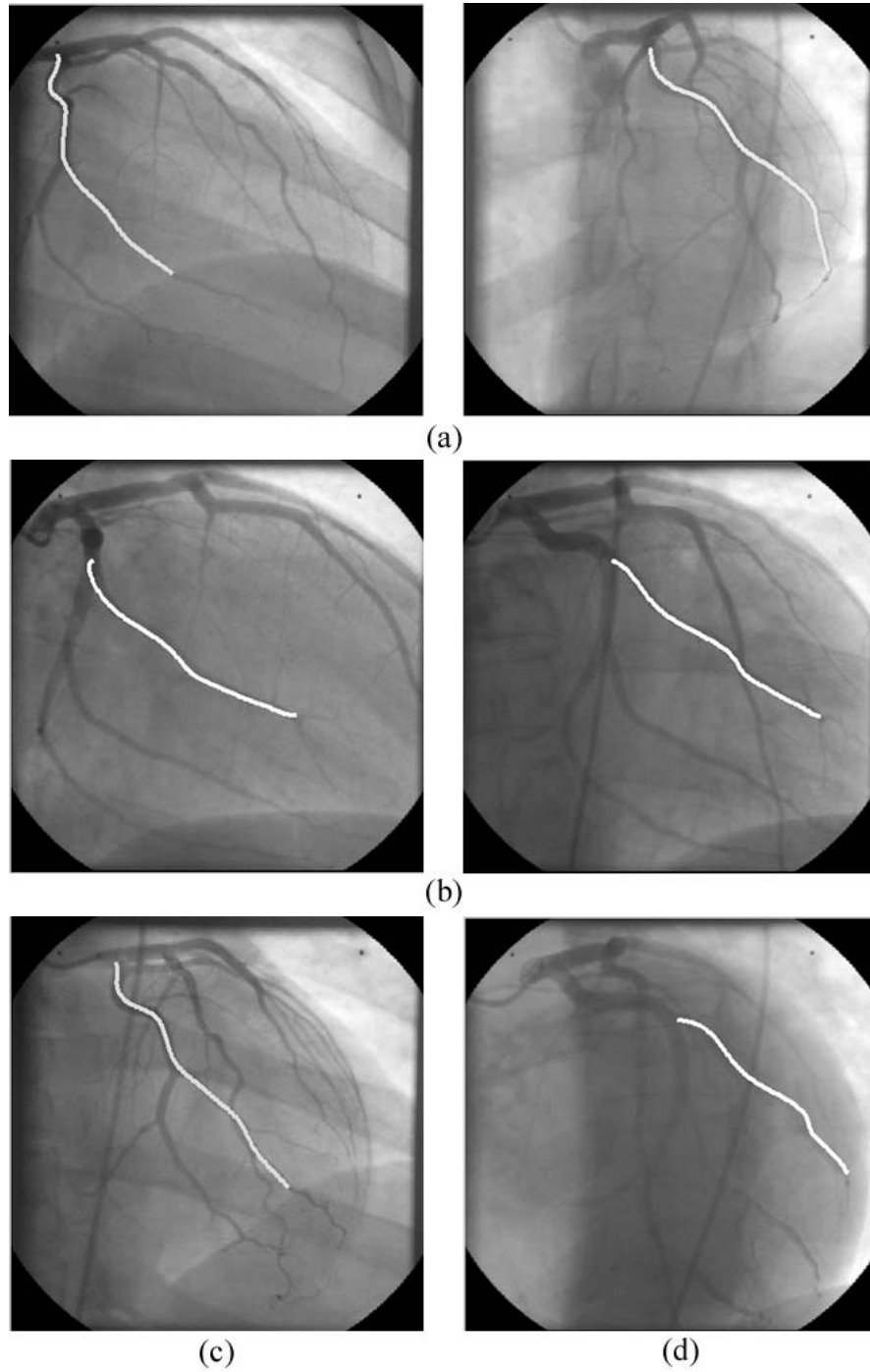


Figure 5.16: 3D reconstruction examples on real cardiac images.

5.4.1 Quantitative Evaluation on Synthetic Images

To quantitatively evaluate the de-noising performance of both diffusion filters, we used the Contrast-To-Noise Ratio (CNR). This measure was applied to the original image, to the result obtained using the Crease Enhancement Diffusion filter defined by Solé et al. in [85] and to the obtained one after applying the Vesselness Enhancement Diffusion filter, which is proposed in section 4.2.1 of this thesis.

The Contrast-To-Noise Ratio of the image was used in [58] to evaluate the performance of several filtering techniques to reduce background noise while retaining vessel contrast. The proposed expression for the CNR was the following [58]:

$$\text{CNR} = \left(\frac{\langle I \rangle_\nu - \langle I \rangle_\beta}{\sigma_\beta} \right)^2 \quad (5.1)$$

where $\langle I \rangle_\nu$ is the mean gray-value within the vessel, and $\langle I \rangle_\beta$ and σ_β are the mean and standard deviation of the gray-value on the background, respectively. Since the images are synthetic, we have available the ground-truth regions of the vessel and the background for each image and therefore this measure is easy to compute. However, expression (5.1) does not take into account the noise on the vessel. Hence, this expression is not a fair measure to evaluate the performance of our denoising filter, since we are only smoothing the vessels, and therefore the background standard deviation is not modified.

Instead, we estimated the Contrast-to-Noise Ratio as follows:

$$\text{CNR} = \left(\frac{\langle I \rangle_\nu - \langle I \rangle_\beta}{\sigma_n} \right)^2 \quad (5.2)$$

where σ_n is the standard deviation of the noise on the whole image. This is actually the Contrast-to-Noise measure described in [83]. Let N_ν , N_β be the number of pixels of the region corresponding to a vessel and to the background, respectively, and σ_ν be the standard deviation of the gray-value in the vessel. We can estimate the standard deviation of the noise σ_n as follows:

$$\sigma_n = \sqrt{\frac{N_\nu \sigma_\nu^2 + N_\beta \sigma_\beta^2}{N_\nu + N_\beta}}$$

Synthetic Images Generation

To generate images of synthetic vessels, we proceed as follows. First, we randomly generated the vessel centerline of the desired vessel on the image. Then, we computed the distance map $d(u, v)$ to the vessel centerline on the image. After, we computed the following expression for each pixel (u, v) on the image $I(u, v)$:

$$I(u, v) = \begin{cases} 0 & \text{if } d(u, v) > R \\ B - \frac{V}{R} \sqrt{R^2 - d(u, v)^2} & \text{otherwise} \end{cases}$$

where parameter R is the radius of the vessel on the image, parameter V is the maximum intensity of the vessel at the vessel centerline and parameter B is the mean

background level. This model is inspired in the model proposed by Kitamura et al. in [45]. Figure 5.17 illustrates the meaning of each parameter. Finally, we added gaussian noise with standard deviation η to the image.

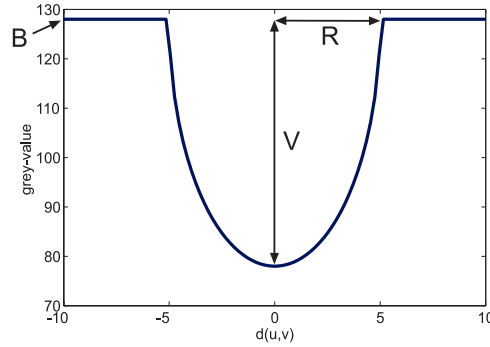


Figure 5.17: Vessel model used to create the synthetic images.

Using this method, we synthesized three types of images. The first type of images contained only one vessel. The second type of images contained a bifurcated vessel, with the main vessel of a higher scale than the other one. The third type was as the second type but adding low-contrasted vessels to simulate background structures. We also added gaussian noise to all the obtained images, for different values of standard deviation η . Figure 5.18 shows an example for each of the three types of synthetic images.

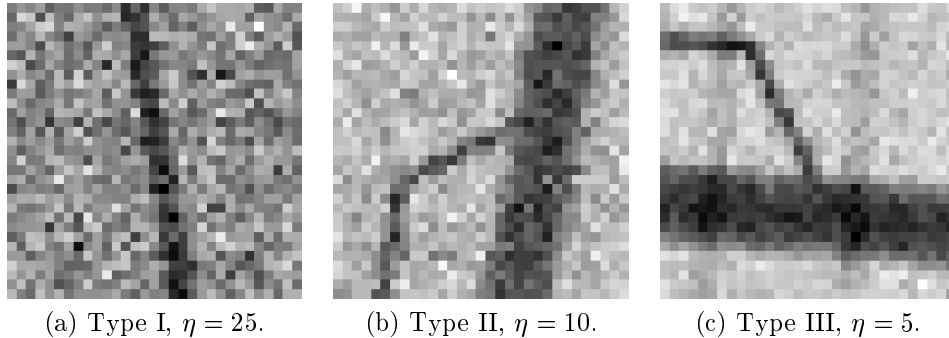


Figure 5.18: Three types of synthetic images used to evaluate our filter.

Experiments on Isolated Vessels

We generated 100 synthetic images containing an isolated vessel with radius $R = 2$, $B = 128$ and $V = 50$ for different values of noise $\eta = \{5, 10, 15, 20\}$. Hence, we obtained 400 images. For each of these images, we iterated 100 times the CED filter with $\alpha = 0$, $\beta = 1$, $\rho = 0.5$, $\epsilon = 0.01$ and $\sigma = 3$. For each synthetic image we also

iterated the VED filter proposed by us 100 times using $\rho = 0.5$, $\sigma = \{2, 3, 4\}$, $\epsilon = 0.01$ and $\theta = 0.5$.

To evaluate the performance of the filtering methods, we computed the Contrast-to-Noise Ratio from equation (5.2) for each synthetic image (without pre-processing) and also for the filtered ones. Figure 5.19 illustrates the results obtained. Note that the CED filtering in general enhances the image, since the mean computed CNR is higher. However, for high values of noise strength η , the CNR is in some cases deteriorated. On the other hand, the VED filter attains much better results, and hence seems to perform the best.

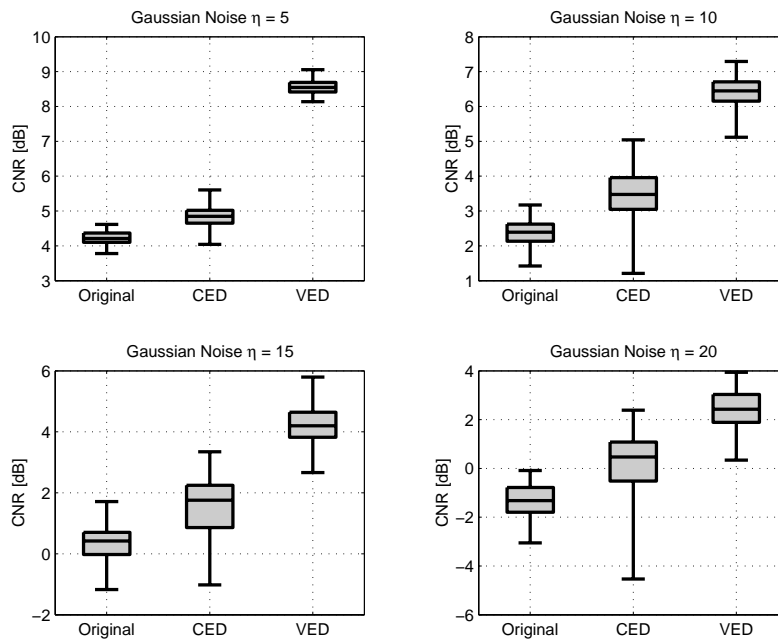


Figure 5.19: Contrast-to-Noise Ratio computed on the gray-scale image for different values η of noise strength (isolated vessels).

To test whether the vesselness measure was also improved, we computed the Contrast-to-Noise Ratio on the vesselness computed for each synthetic image (without pre-processing) and also for the filtered ones. Figure 5.19 shows the results obtained. Note that by pre-processing the image using the CED filter, we can obtain worse results than when no pre-processing is applied. On the other hand, pre-processing the image using the VED filter improves the Contrast-to-Noise Ratio of the vesselness on the images.

Experiments on Bifurcated Vessels

We generated 100 synthetic images containing a bifurcated vessel, with the main vessel of a higher scale than the other, for different values of noise $\eta = \{5, 10, 15, 20\}$. The scale of the radius of the main vessel was randomly selected to be in the range

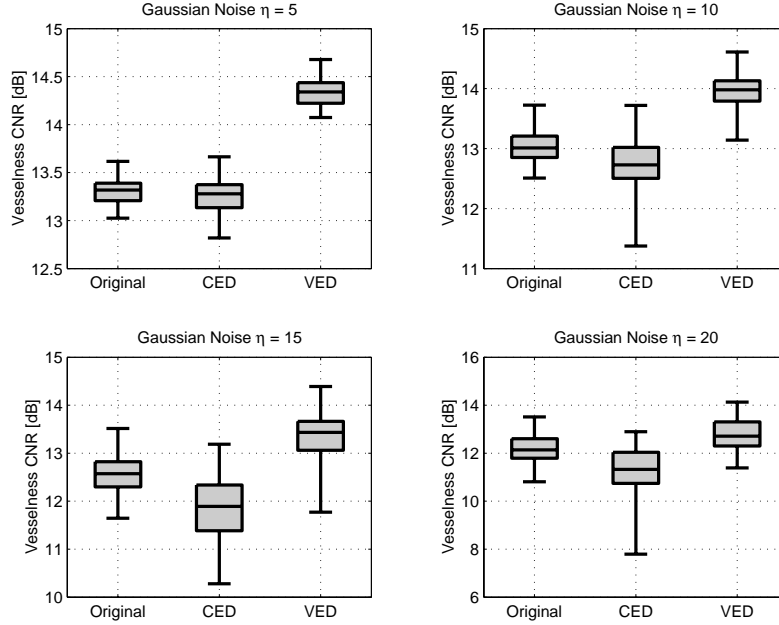


Figure 5.20: Contrast-to-Noise Ratio computed on the vesselness image for different values η of noise strength (isolated vessels).

$R \in [3, 5]$, and the other vessel had radius $R \in [1, 2]$. Both vessels were generated using $B = 128$ and $V = 50$. Hence, we obtained 400 images. For each of these images, we iterated 100 times the CED filter with $\alpha = 0$, $\beta = 1$, $\rho = 0.5$, $\epsilon = 0.01$ and $\sigma = 3$. For each synthetic image we also iterated the VED filter proposed by us 100 times using $\rho = 0.5$, $\sigma = \{2, 3, 4\}$, $\epsilon = 0.01$ and $\theta = 0.5$.

As in the previous experiment, we measured the Contrast-to-Noise Ratio for each synthetic image (without pre-processing) and also for the filtered ones. Results are shown in figure 5.21. Note that the best CNR results were obtained using the VED filter. Also, we tested the influence of the filtering on the CNR computed on the vesselness. Results in figure 5.22 show that pre-processing using the CED filter can deteriorate the performance of the vesselness measure. On the other hand, using the VED filter as a pre-processing step provides an improved vesselness measure.

Experiments with Background Structures

We generated 400 synthetic images with bifurcated vessels, as done in the previous section, but now we also added two low-contrasted vessels simulating background structures, such as the introduced by the ribs. For each of these images, we iterated 100 times the CED filter with $\alpha = 0$, $\beta = 1$, $\rho = 0.5$, $\epsilon = 0.01$ and $\sigma = 3$. For each synthetic image we also iterated the VED filter 100 times using $\rho = 0.5$, $\sigma = \{2, 3, 4\}$, $\epsilon = 0.01$ and $\theta = 0.5$.

As in the previous experiments, we measured the Contrast-to-Noise Ratio for each

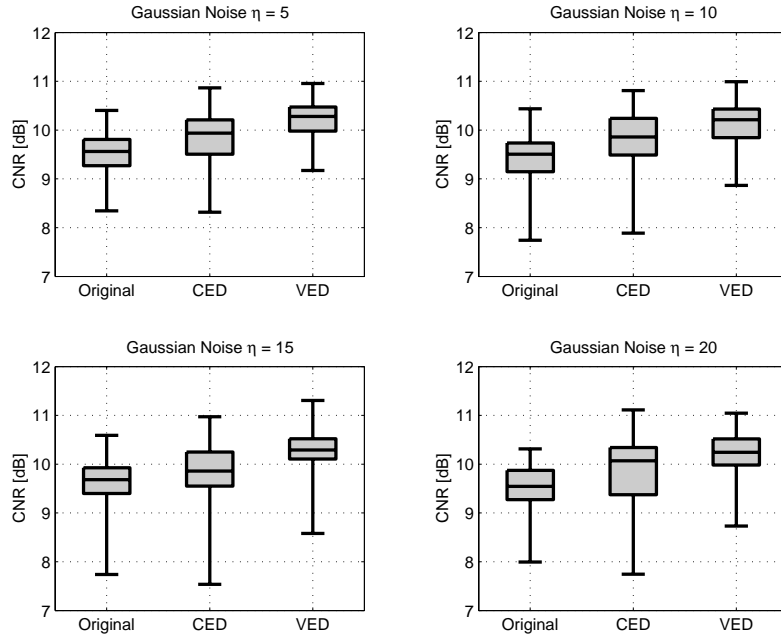


Figure 5.21: Contrast-to-Noise Ratio computed on the gray-scale image for different values η of noise strength (bifurcated vessels).

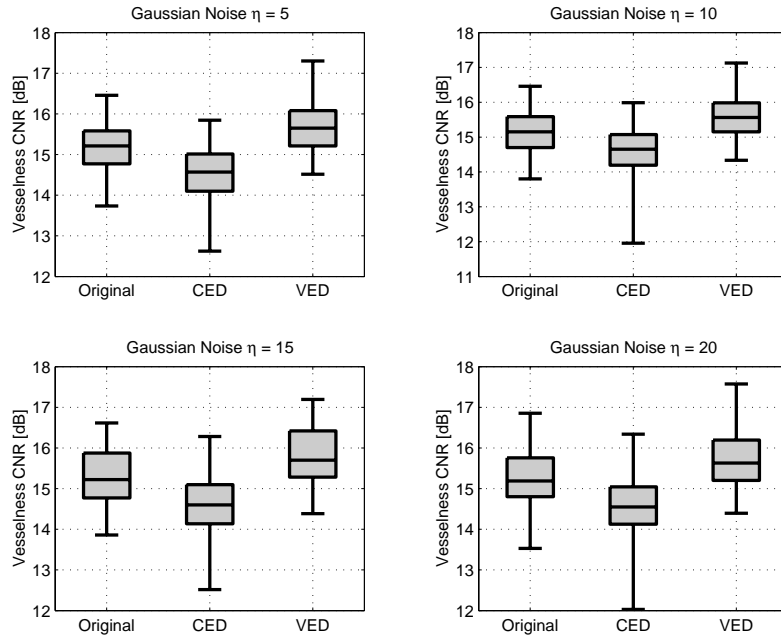


Figure 5.22: Contrast-to-Noise Ratio computed on the vesselness image for different values η of noise strength (bifurcated vessels).

synthetic image (without pre-processing) and also for the filtered ones. Results are shown in figure 5.21. Note that the best CNR results were obtained using the VED filter. Also, we tested the influence of the filtering on the CNR computed on the vesselness. Results in figure 5.22 show that pre-processing using the CED filter in general deteriorates the performance of the vesselness measure, since it also enhances undesired background structures. On the other hand, using the VED filter as a pre-processing step provides an improved vesselness measure.

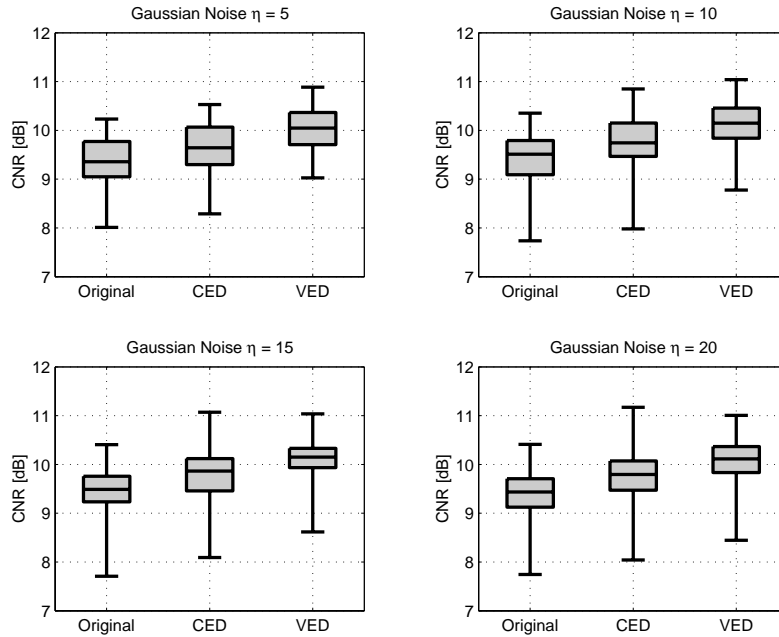


Figure 5.23: Contrast-to-Noise Ratio computed on the gray-scale image for different values η of noise strength (bifurcated vessels + background structures).

5.4.2 Tests on Real Images

In the previous section, we quantitatively measured the performance of the Vessel Enhancement Diffusion filter. However, all the tests were performed on synthetic images. Hence, in this experiment we carried out experiments on real cardiac images containing vessels of different sizes.

For Frangi's vesselness measure, we used $\alpha = 0.5$, $\beta = 0.5$ and half the Hessian norm for c , as indicated in [34]. For the CED filter, we chose $\alpha = 0$ and $\beta = 1$ (in order to only enhance the valleys) and $\epsilon = 0.01$. Finally, for the VED filter we always used $\epsilon = 0.01$ and $\theta = 0.5$. The number of iterations was 100 for both diffusion filters. Regarding the scales used for each method, we have chosen $\sigma = \{1, 1.5, 2, 2.5, 3, 5\}$ for Frangi's filter and for the VED filter. For the CED filter, we have chosen a scale of $\sigma = 2.5$, corresponding to the mean of the scales used with the other methods.

Figure 5.25 shows the results obtained for a ROI on one of the images. Using the

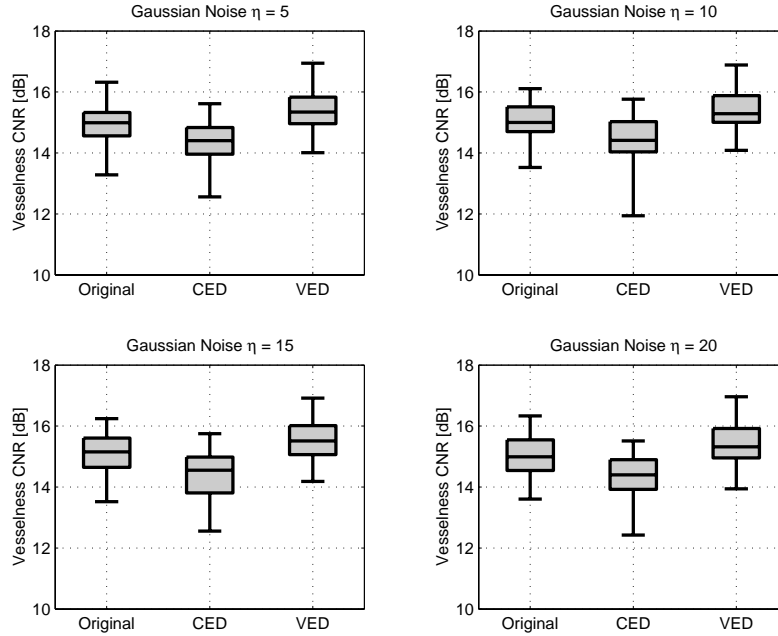


Figure 5.24: Contrast-to-Noise Ratio computed on the vesselness image for different values η of noise strength (bifurcated vessels + background structures).

VED filter, the obtained segmentation is less noisy. Note that the CED filter also enhanced some undesired background structures, whereas some of them had been smoothed. Figure 5.26 shows another example. Using our filter, the vessel contrast has been enhanced on the gray scale image and the segmentation result is more clean. Although we have not smoothed the background, the vesselness background is smoother when using VED filter. We explain this by the higher CNR of the vessels on the image, which facilitates the background removal task to the vesselness measure.

The results obtained encourage us to say that Vessel Enhancement diffusion is a good choice to improve the quality of X-ray images, and can be used to obtain better vessel segmentation results.

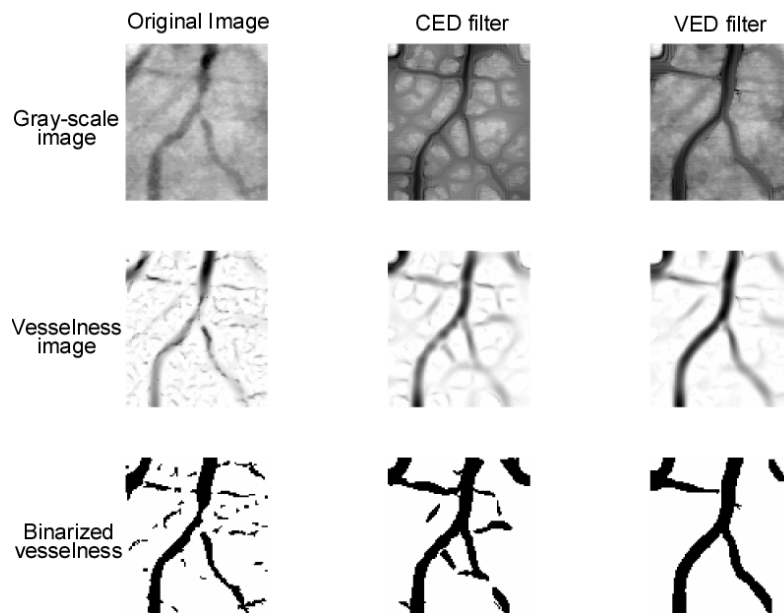


Figure 5.25: Results on a ROI of one of the images.

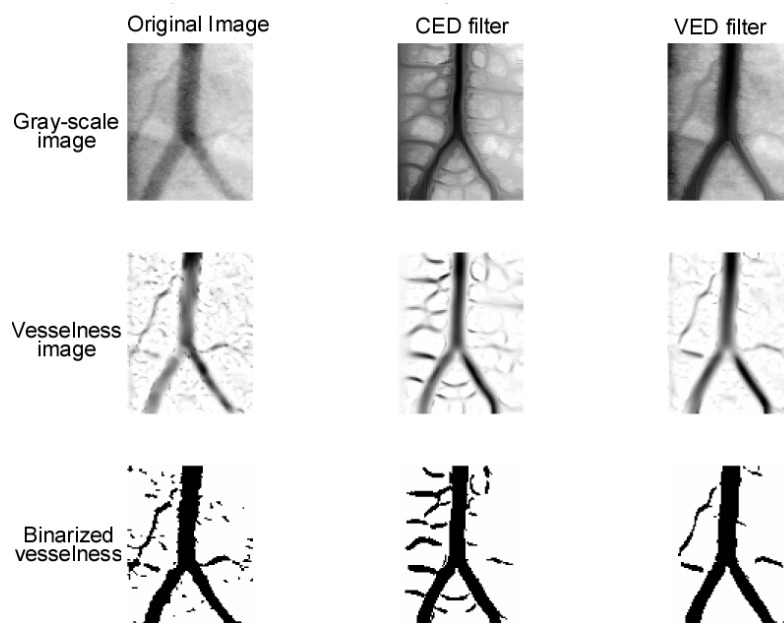


Figure 5.26: Results on a ROI of another of the images.

Chapter 6

Conclusion

In this thesis we have focused on the three-dimensional reconstruction of coronary vessels considering all problems that arise on the road: The geometrical distortion introduced by the image intensifier, the acquisition geometry determination, the automatic vessel detection in images, and three-dimensional reconstruction, without using explicit determination of corresponding points. We have studied each of these problems in this thesis, and made several contributions for each of them.

6.1 Geometrical Distortion

When approaching the three-dimensional reconstruction of the coronary vessels, we find that angiographic images suffer from geometrical distortion, which is introduced by the image intensifier. The main difficulty is that, unlike the distortion introduced by the optics in the camera frame, the distortion introduced by the image intensifier depends, among other things, on the orientation of the image intensifier in relation to the Earth's magnetic field. Therefore, for each projection angle, we will have a different distortion.

We have analysed the geometrical distortion introduced by the Image Intensifier and the different elements that have influence on it, using a calibration grid attached to the Image Intensifier screen. We showed that the geometrical distortion introduced by the Image Intensifier can be accurately modeled by a polynomial for each view. Also, we showed that the estimated polynomial is independent of focal length, but not of changes on anatomical angles, as the Image Intensifier is influenced by the Earth's magnetic field. Thus, we decomposed the polynomial in two components, namely the steady and the orientation-dependent component. We determined the optimal polynomial degree for each component: 5 for the steady component, 3 for the orientation-dependent one and 4 for the polynomials which estimate each of the coefficients of the polynomials modelling the orientation-dependent component.

Experiments showed that the mean error obtained with the estimated polynomials using this procedure is less than 0.3 pixels, which equals to less than 0.1mm at the Image Intensifier screen. Note that this error is a superior bound. Near the heart, the error will be attenuated by approximately 2/3.

Hence, we have developed an accurate model for image distortion, which eliminates the requirement of geometrical distortion calibration at each acquisition.

6.2 Determination of the Acquisition Geometry

We have analysed the assumptions made by Dumay's model [22], which are that the image is perfectly aligned with \mathbf{k} and \mathbf{l} , that the rotation axis and the angulation axis do intersect, that the rotation axis and the angulation axis are orthogonal, and that the central beam is orthogonal to the angulation axis. As an alternative, we have proposed new models (**M1**, **M2**, **M3** and **M4**) to estimate the extrinsic parameters, which take into account these facts.

Then, we have proposed a method to calibrate the parameters of the proposed models by using a calibration object which is commonly available by the physicians, since it is the calibration grid used to estimate geometrical distortion. Moreover, the calibration procedure is very flexible, since the only requirements are that the distance between the X-ray source and the image intensifier must remain constant between all the calibration acquisitions and that the grid must be on the table at a fixed position. Both requirements are very easy to fulfill and therefore the calibration procedure is very easy to perform.

Experimental results led us to believe that our models perform better than the traditional isocentric model. In particular, experiments showed that by combining the distortion model proposed by us and model **M4** for the extrinsic parameters we obtain a mean three-dimensional reconstruction error projected on the images of less than one pixel, with a maximum error of less than 5.5 pixels for the test set. This result is much better than the obtained with the classical isocentric model, where the mean error is of 5.63 pixels and the maximum up to 23 pixels for the test set. Moreover, we have shown that when reconstructing a three-dimensional wire phantom, the accuracy obtained using model **M4** remains acceptable even three-months after the calibration procedure.

These results encourages us to state that by using the proposed new model **M4** to estimate the extrinsic parameters, it shall not be necessary a calibration nor a refinement at each acquisition, as proposed in [23, 13, 28], but only a periodic calibration. This fact is very important, since it highly simplifies the clinical application of diagnostic techniques involving 3D reconstruction from angiographies.

6.3 Automatic Vessel Detection

One of the most difficult problems when approaching the 3D reconstruction of the vessels is the automatic vessel segmentation. The main difficulty relies on the fact that X-ray cardiac angiographies are very noisy, and small vessels with low contrast are hard to detect.

We have proposed a new anisotropic diffusion filter to enhance the vessels on the X-ray angiographic images. The proposed filter uses a diffusion tensor inspired in the crease enhancement diffusion filter proposed by Solé et al. in [85], but here the diffusion strength is determined by the vesselness measure defined by Frangi et al. in [34]. Moreover, our filter chooses for each pixel the scale of the diffusion tensor to be applied. This approach performs better than the crease enhancement diffusion filter to enhance the vessels, since our approach is multi-scale and therefore can deal with multiple vessel sizes. Moreover, our approach only enhances contrasted vessels, and therefore background structures are not enhanced, as the crease enhancement diffusion filter does. Compared to the performance of only using the vesselness measure to detect the vessels, our approach takes into account image coherence, i.e. if a pixel is considered to be part of a vessel, the neighbour pixel in the direction of the vessel is very likely to correspond also to a vessel. Hence, the resulting image is an enhanced one, which gives a better response to the vesselness measure, allowing a more robust vessel segmentation.

6.4 Automatic Corresponding Points Determination

To obtain the three-dimensional reconstruction of coronary vessels, the usual approach consists on reconstructing corresponding points in both X-ray images, and then obtaining a 3D curve by interpolation between the obtained 3D points. However, automatic correspondence determination may be computationally expensive and it must deal with ambiguities. The usual approach is therefore asking the user to manually mark corresponding points. This task is also non-trivial for the user, and can become quite tedious if high accuracy is needed.

We have proposed the use of a new type of deformable models, biplane snakes, to solve the point correspondence determination problem. We have defined biplane snakes as a three-dimensional curve that deforms in space in order to adapt its projections to the vessels in the images. The initial shape is indicated by the user using some initialization points near the vessel to be reconstructed. The acquisition views can be not orthogonal, although it is always recomendable to have a minimum angulation between the two reconstruction views in order to obtain good accuracy results. Experimental results show that by using biplane snakes, the obtained three-dimensional reconstruction is at least as good as a human user would obtain. Moreover, when the acquisition conditions are not known with high accuracy, biplane snakes obtain better results.

To improve the performance of biplane snakes when reconstructing wavy vessels,

we have proposed the use of the GGVF as external force. Also, we have included the (un)distortion model proposed by us in the snake deformation formulation. Hence, it is not necessary to unwarp the image in order to obtain an accurate three-dimensional reconstruction. Experiments show that by including the distortion model on the snake deformation formulation, the 3D reconstruction error is decreased up to an 88% versus the obtained one when distortion is ignored.

Finally, we have validated the technique with imaged phantoms and real angiographic sequences acquired with a monoplane angiographic system. Experiments show that long complex shapes and overlapping vessels can be reconstructed by simply adding a few extra initialization points to help the snake to converge to the desired target.

6.5 Applications

The three-dimensional reconstruction from X-ray angiography has many interesting applications:

- From two views, we can reconstruct the catheter path, which is needed for the fusion of X-ray angiography and IntraVascular UltraSound images. X-ray coronary angiography presents the lack of the foreshortening effect when evaluating the degree of a stenosis, while IVUS has the problem of an excessive locality of the information that they provide. The fusion between the information provided by the angiography (the 3D catheter path) and the one provided by the IVUS (the cross-sectional transmural data) is therefore a good choice, since the result obtained allows a global assessment of the vessel lesion, by means of volumetric measurements and 3D visualizations. Examples of the fusion of X-ray angiography and IVUS can be found in [73, 93, 78].
- Since using our proposals we can obtain an accurate three-dimensional reconstruction of a vessel segment, we can use the three-dimensional reconstruction to measure the size of a lesion. An example of this application can be found in [8].
- By tracking the reconstructed three-dimensional vessel along a complete cardiac cycle, we can obtain information about the dynamics of the vessel of interest, which is very useful for diagnostic purposes. An example of this application can be found in [90].
- The three-dimensional reconstruction of a vessel segment can also be used to determine the optimal views to acquire it. These views shall be two perpendicular ones that are both parallel to the main axis of the vessel. An examples of a work on this issue is [22].

6.6 Suggesting New Directions of Study

During our study on the three-dimensional reconstruction of coronary vessels from X-ray angiography, different possible lines of continuation have been formulated:

- The authors in [63] claim that the high weight of the Image Intensifier can cause some bending on the C-arm. This bending would affect the intrinsic parameters, especially the image center (u_0, v_0) . Hence, it would be of interest to study the behaviour of the intrinsic parameters for different orientations of the C-arm, and different distances from the X-ray source to the image intensifier and, if necessary, to develop a model to estimate the intrinsic parameters for any view.
- We have shown that the Vesselness Enhancement Diffusion filter proposed in this thesis improve the Contrast-to-Noise Ratio of the vesselness measure, and therefore, it facilitates vessel segmentation. However, the background is not modified using this filter, and hence background noise and undesired structures are not smoothed on the gray-scale image. Therefore, another line of continuation would be to develop an improved filter that also includes this feature. Another improvement would be to also enhance the edges of the vessels, which would be very interesting for some Quantitative Coronary Angiography applications, as the stenosis measurement.
- The extraction of the vessel centerline has been done using a crease detector. Although the chosen solution performs quite well, in the presence of wavy vessels the technique fails in finding the correct vessel centerline. Hence, a deeper study on vessel centerline extraction should be done.
- Experimental results presented in this thesis encourages us to state that by using the proposed new model **M4** to estimate the extrinsic parameters, it shall not be necessary a calibration nor a refinement at each acquisition. Thus, another continuation guideline would be to quantitatively evaluate the accuracy deterioration along time of this model to know for how many time the model is accurate.
- The introduction of the GGVF as external force on the biplane snakes formulation improved the performance of biplane snakes when reconstructing wavy vessels. However, computing the GGVF has a high computational cost. Hence, the study of alternatives to the GGVF is also a continuation guideline.

Appendix A

Matrix Representation for Deformable Models

In this appendix, we present the deformable models implementation details. We have chosen a matrix representation, since it is specially well-suited for implementation on a matrix manipulator as MATLAB(tm), or with any matrix library. Moreover, this representation is very compact and therefore should help the reader to understand how this model works.

We present the matrix representation for one-dimensional and two-dimensional deformable models. For higher dimensional deformable models, a tensorial representation would be necessary.

A.1 One-Dimensional Deformable Models (B-Snakes)

The one-dimensional deformable models have the following expression:

$$Q(u) = \sum_i V_i B_i(u)$$

And, developping from (2.27), the internal energy is re-written as follows:

$$\begin{aligned} E_{int}(Q) &= \alpha \int \left(\frac{\partial Q(u)}{\partial u} \right)^2 du + \beta \int \left(\frac{\partial^2 Q(u)}{\partial^2 u} \right)^2 du \\ &= \alpha \int \left(\sum_i V_i B_i'(u) \right)^2 du + \beta \int \left(\sum_i V_i B_i''(u) \right)^2 du \quad (\text{A.1}) \end{aligned}$$

For one-dimensional B-Splines, we can use Blake's matrix notation [3]. A B-spline curve $Q(u)$ of degree d (for cubic splines, $d = 4$) and M control points, is defined parametrically for $0 \leq u \leq N$, where $M = N$ for closed curves and $M = N + d$ for open ones (with appropriate variations where multiple knots are used to vary curve continuity):

$$Q(u) = \sum_i V_i B_i(u) = \mathbf{B}(u) \mathbf{V} = \mathbf{B}(s + \sigma) \mathbf{V} = \begin{pmatrix} 1 & s & \dots & s^{d-1} \end{pmatrix} B_\sigma^S G_\sigma \mathbf{V} \quad (\text{A.2})$$

where $0 \leq s < 1$. \mathbf{V} is a $M \times 1$ matrix containing the control points, B_σ^S is the $d \times d$ standard B-spline matrix corresponding to the σ -span and G_σ is a $d \times M$ matrix that simply selects d consecutive control points:

$$G_n \mathbf{V} = (V_n \ \dots \ V_{n+d})^T \quad 1 \leq n \leq N \quad (\text{A.3})$$

Note that, for a closed curve, control point indexes are evaluated modulo M .

A.1.1 B-Spline Inner product

Blake [3] defines an inner product and thus a norm for the splines via a metric matrix \mathcal{B} :

$$\|Q(u)\|^2 = \int Q(u)Q(u)du = \mathbf{V}^T \mathcal{B} \mathbf{V}$$

where \mathcal{B} is defined as:

$$\mathcal{B} = \frac{1}{L} \int_0^L \mathbf{B}(u)^T \mathbf{B}(u) ds$$

and developping:

$$\begin{aligned} \mathcal{B} &= \frac{1}{L} \sum_{\sigma=0}^{L-1} \left(\int_0^1 \mathbf{B}(s+\sigma)^T \mathbf{B}(s+\sigma) ds \right) \\ &= \frac{1}{L} \sum_{\sigma=0}^{L-1} G_\sigma^T B_\sigma^S{}^T \mathcal{P} B_\sigma^S G_\sigma \end{aligned}$$

where

$$\mathcal{P} = \int_0^1 \begin{pmatrix} 1 \\ \vdots \\ s^{d-1} \end{pmatrix} (1 \ \dots \ s^{d-1}) ds, \quad (\text{A.4})$$

is the "Hilbert" matrix whose coefficients are:

$$\mathcal{P}_{ij} = \frac{1}{i+j-1}$$

A.1.2 Stiffness Matrix

If we use the form (A.2) the first and second derivatives of the splines can be calculated as:

$$\begin{aligned} Q'(u) &= \mathbf{B}'(s+\sigma) \mathbf{V} = (0 \ 1 \ \dots \ (d-1)s^{d-2}) B_\sigma^S G_\sigma \mathbf{V} \\ Q''(u) &= \mathbf{B}''(s+\sigma) \mathbf{V} = (0 \ 0 \ 2 \ \dots \ (d-2)(d-1)s^{d-3}) B_\sigma^S G_\sigma \mathbf{V} \end{aligned}$$

We can easily define:

$$\begin{aligned}
E_{int}(Q) &= \alpha \int Q'(u)^2 du + \beta \int Q''(u)^2 du \\
&= \alpha \int_0^L \mathbf{V}^T \mathbf{B}'(u)^T \mathbf{B}'(u) \mathbf{V} du + \beta \int_0^L \mathbf{V}^T \mathbf{B}''(u)^T \mathbf{B}''(u) \mathbf{V} du \\
&= \alpha \mathbf{V}^T \mathcal{B}' \mathbf{V} + \beta \mathbf{V}^T \mathcal{B}'' \mathbf{V}
\end{aligned} \tag{A.5}$$

where \mathcal{B}' and \mathcal{B}'' are defined as:

$$\mathcal{B}' = \frac{1}{L} \sum_{\sigma=0}^{L-1} G_{\sigma}^T B_{\sigma}^{S^T} \mathcal{P}' B_{\sigma}^S G_{\sigma} \quad \mathcal{B}'' = \frac{1}{L} \sum_{\sigma=0}^{L-1} G_{\sigma}^T B_{\sigma}^{S^T} \mathcal{P}'' B_{\sigma}^S G_{\sigma}$$

with

$$\mathcal{P}' = \int_0^1 \begin{pmatrix} 0 \\ 1 \\ \dots \\ (d-1)s^{d-2} \end{pmatrix} (0 \ 1 \ \dots \ (d-1)s^{d-2}) ds$$

and

$$\mathcal{P}'' = \int_0^1 \begin{pmatrix} 0 \\ 0 \\ 2 \\ \dots \\ (d-2)(d-1)s^{d-3} \end{pmatrix} (0 \ 0 \ 2 \ \dots \ (d-2)(d-1)s^{d-3}) ds$$

Note that matrices \mathcal{P}' and \mathcal{P}'' can be accurately computed as follows:

$$\mathcal{P}'_{ij} = \begin{cases} 0 & \text{if } i = 1 \text{ or } j = 1 \\ \frac{(i-1)(j-1)}{i+j-3} & \text{otherwise} \end{cases}$$

$$\mathcal{P}''_{ij} = \begin{cases} 0 & \text{if } i < 3 \text{ or } j < 3 \\ \frac{(2-3i+i^2)(2-3j+j^2)}{i+j-5} & \text{otherwise} \end{cases}$$

At this point, expressing the internal energy from equation (A.1) using matrix notation is of interest:

$$\begin{aligned}
E_{int}(\mathbf{V}) &= \alpha \mathbf{V}^T \mathcal{B}' \mathbf{V} + \beta \mathbf{V}^T \mathcal{B}'' \mathbf{V} \\
&= \mathbf{V}^T (\alpha \mathcal{B}' + \beta \mathcal{B}'') \mathbf{V} \\
&= \mathbf{V}^T \mathcal{H} \mathbf{V}.
\end{aligned} \tag{A.6}$$

The matrix \mathcal{H} corresponds to the B-Spline version of the so-called *stiffness* matrix which appears in the energy minimization procedure presented in [42]

Therefore, the *stiffness* matrix \mathcal{H} can be computed as:

$$\mathcal{H} = \frac{1}{L} \sum_{\sigma=0}^{L-1} G_{\sigma}^T B_{\sigma}^{S^T} (\alpha \mathcal{P}' + \beta \mathcal{P}'') B_{\sigma}^S G_{\sigma} \quad (\text{A.7})$$

This matrix provides an efficient way to calculate the internal energy. Since the only change is the value of the control points, the only operation we are supposed to do at each iteration is two matrix multiplications in order to compute the internal energy.

A.1.3 Energy-Minimization Algorithm

From the work of Kass et al. [42], the equation corresponding to the one-dimensional case of the energy-minimization algorithm is:

$$\mathbf{V}_t = (\mathbf{A} + \gamma \mathbf{I})^{-1} (\gamma \mathbf{V}_{t-1} - \mathbf{f}(\mathbf{V}_{t-1}))$$

Where \mathbf{V}^t is the discretization of the curve at time t , \mathbf{A} is the *stiffness* matrix, $\mathbf{f}(\mathbf{V}^{t-1})$ is the finite difference approximation of $F(Q(u)) = \nabla E_{ext}(Q(u))$ (the external force is the spatial gradient of the external energy) and γ is the time step size.

When working with B-Snakes, the energy-minimization procedure is very similar:

$$\mathbf{V}_t = (\mathcal{H} + \gamma \mathbf{I})^{-1} (\gamma \mathbf{V}_t - \mathbf{g}(Q_{t-1}))$$

The difference is subtle, but important. Instead of datapoints, \mathbf{V}_t represents the control points of the B-Spline, and \mathbf{g} assigns to each control point the corresponding external force taking into account its influence over the curve at each point of the curve. It is defined as:

$$[\mathbf{g}(Q)]_i = \int B_i(u) F(Q(u)) du$$

Since in most cases we can only have a discrete form of $F(Q(u))$ because of the discrete nature of the images, a discretization of this expression is done as follows:

$$[\mathbf{g}(Q)]_i = \frac{1}{p} \sum_{k=0}^p B_i(u_k) F(Q(u_k))$$

A.2 Two-Dimensional Deformable Models (B-Sheets)

For two-dimensional models we use the following expression:

$$Q(u, v) = \sum_i \sum_j V_{ij} B_i(u) B_j(v) \quad (\text{A.8})$$

By using this expression, three simple topologies- planar, cylindrical and toroidal- can be represented. When both u and v functions are open, we obtain a planar

topology, whereas if both are closed, we obtain a toroidal surface. If only one of the functions are closed, then we can represent a cylindrical topology.

Using Blake's notation[3], a B-spline sheet $Q(u, v)$ of degrees d_u and d_v and $M_u \times M_v$ control points is parametrically defined for $0 \leq u \leq N_u$ and $0 \leq v \leq N_v$ as:

$$Q(u, v) = Q(s_u + \sigma_u, s_v + \sigma_v) = \begin{pmatrix} 1 & \dots & s_u^{d_u-1} \end{pmatrix} B_{\sigma_u} G_{\sigma_u} \mathbf{V} G_{\sigma_v}^T B_{\sigma_v}^T \begin{pmatrix} 1 \\ \vdots \\ s_v^{d_v-1} \end{pmatrix} \quad (\text{A.9})$$

where $0 \leq s_u < 1$ and $0 \leq s_v < 1$. \mathbf{V} is a $M_u \times M_v$ matrix containing the control points, B_{σ_u} , B_{σ_v} are standard B-spline matrices and G_{σ_u} , G_{σ_v} selection matrices.

A.2.1 Energy Minimization Algorithm

It has been empirically confirmed in [75] that given γ close to unity, the energy minimization procedure for the B-Sheets can be reduced to an expression similar to those of the B-Snakes and can also be expressed in matrix form as follows:

$$\mathbf{V}_t = (\mathcal{H}_u + \gamma \mathbf{I})^{-1} (\gamma V_{t-1} - \mathbf{g}(Q_{t-1}(u, v))) (\mathcal{H}_v + \gamma \mathbf{I})^{-1}$$

Where \mathcal{H}_u and \mathcal{H}_v are the *stiffness* matrices corresponding to the parameters α_u , β_u and α_v , β_v respectively. For the two dimensional case, $\mathbf{g}(Q_{t-1}(u, v))$ is defined as follows:

$$[\mathbf{g}(Q)]_{ij} = \int \int B_j(v) B_i(u) F(Q(u)) du dv$$

Like in the one-dimensional case, in most cases we can only have a discrete form of $F(Q(u))$. Here the discrete form is:

$$[\mathbf{g}(Q)]_{ij} = \frac{1}{p_u p_v} \sum_{k_2=0}^{p_v} \sum_{k_1=0}^{p_u} B_j(v_{k_2}) B_i(u_{k_1}) F(Q(u_{k_1}, v_{k_2}))$$

Where p_u, p_v are the number of sampled points for each internal parameter. Note that we will sample $p_u p_v$ points.

Appendix B

Crossing points detection

Once the calibration grid is fixed on the II, different images are acquired B.1(a). A morphological operation (gray-scale closure with a square-shaped structural element) is then applied to eliminate the grid, obtaining the background (figure B.1(b)) and the lighting variation of the image. By subtracting the background from the original image we obtain the grid (figure B.1(c)). Then, a closure with a horizontal/vertical structural element isolates horizontal/vertical wires (figures B.1(d) and B.1(e)). Thresholding can then be applied to obtain a binary image. The thresholding value is chosen by a standard histogram based method, like the Otsu's method [70]. Crossing points correspond to the intersection of the detected horizontal and vertical wires (see figure B.1(f)).

Since horizontal and vertical wires are decoupled, the physical location (\mathbf{x}, \mathbf{y}) of the crossing points ($\hat{\mathbf{u}}, \hat{\mathbf{v}}$) detected on the images is now very easy to obtain. First, we compute the center of mass of each wire and then we sort them by the x component the vertical wires and by the y component the horizontal ones. Since crossing point regions belong to horizontal and vertical wire regions, the mapping is directly the resulting order.

To refine the location of the intersection points from the intersection areas in the images, we explored different approaches:

- *Method 1.* Simply compute the centroids of the resulting crossing areas.
- *Method 2.* Using the centroids obtained by method 1 as starting values, iteratively compute the center of gravity in a small area of the inverted gray-scale image after subtracting the background around the previous position as it stabilizes [38].
- *Method 3.* Compute vertical and horizontal projections of a small region of the inverted gray-scale image after subtracting the background around each of the centroids obtained by method 1 and adapt the following function:

$$f(x) = k_1 e^{-\frac{(x-\mu)^2}{\sigma}} + k_2 \tag{B.1}$$

to each projection by applying a non-linear curve fitting method. Parameter μ

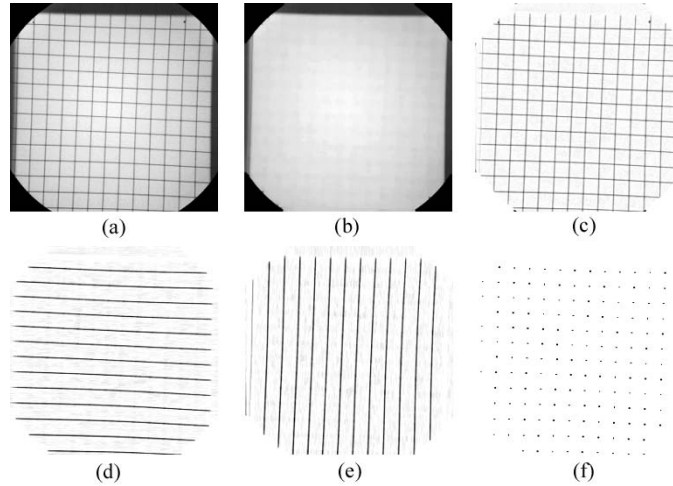


Figure B.1: Crossing points detection using mathematical morphology. Although the grid was mounted regardless of orientation, the crossing points are correctly detected. The detected points are then refined by one of the proposed methods to obtain subpixel accuracy.

provides a robust subpixel estimate of the position of the maximal point for this projection (see figure B.2). Thus, the intersection is located at (μ_x, μ_y) .

To test the calibration accuracy, we performed several experiments using a calibration grid image. Given that our data for the calibration phase are provided by the intersection points of the calibration grid, their accurate extraction is very important to ensure the correctness of the calibration calculus.

B.1 Accuracy on Crossing Points Detection

We implemented the three methods to detect the subpixel position of crossing points on the image. In order to select the most appropriate method, we acquired the calibration grid during 100 frames, without moving the II. Then, crossing points were detected using each of the proposed location methods. Finally, distance from the location of each crossing point to the mean was computed for all methods. As the results show in figure B.3, method 1 has a maximum error of 1 pixel, method 2 gives a maximum error of 0.75 pixels and method 3 results the most accurate method, with a 99% of samples less than 0.1 pixel distance to the mean position of the intersection points.

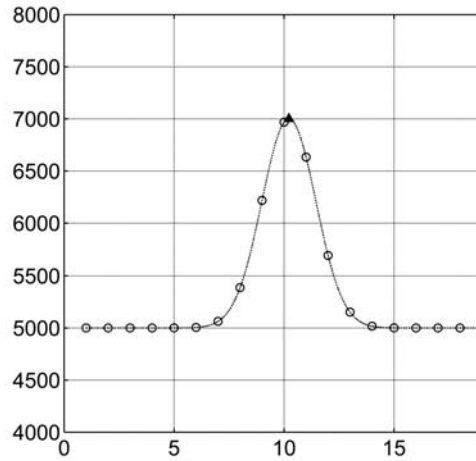


Figure B.2: Function $f(x) = k_1 e^{-\frac{(x-\mu)^2}{\sigma}} + k_2$ fitted to the projection of the intersection areas. The subpixel estimate of the position of the maximal point is marked with a triangle.

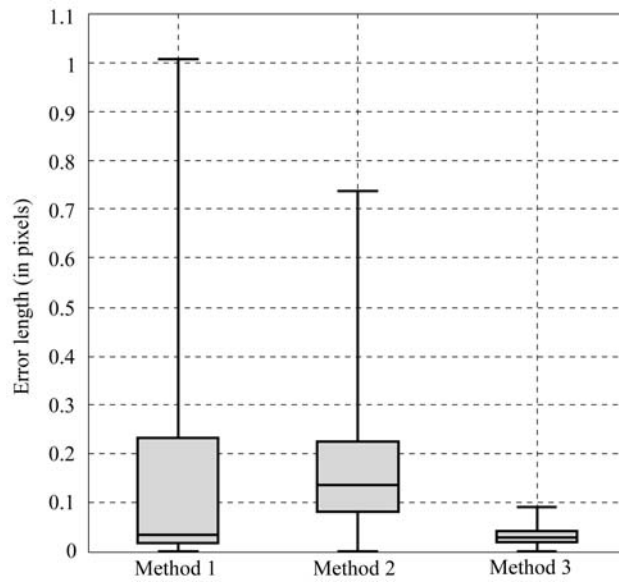


Figure B.3: Error length (in pixels) of the detection of the crossing points for each method.

Appendix C

Bivariate polynomial fitting

Let $[\mathbf{x}, \mathbf{y}]$ be a $m \times 2$ matrix corresponding to the measured data points and \mathbf{z} the $m \times 1$ vector of values at each point. Fitting a bivariate polynomial to this data means finding the coefficients \mathbf{c} of the function:

$$f(x, y, \mathbf{c}) = \sum_{i=0}^n \sum_{j=0}^i \mathbf{c}_k x^{i-j} y^j,$$

where n is the desired degree, $k = \frac{i(i+1)}{2} + j$ and f minimizes the expression:

$$\sum_i (\mathbf{z}_i - f(\mathbf{x}_i, \mathbf{y}_i, \mathbf{c}))^2$$

In fact, this problem can be reduced to a linear least-squares optimization problem, since finding the c_k coefficients (vector \mathbf{c}) can be expressed as the following over-determined linear system:

$$\mathbf{U}\mathbf{c} = \mathbf{z} \tag{C.1}$$

where

$$\mathbf{U} = [\mathbf{x}^n, \mathbf{x}^{n-1}\mathbf{y}, \mathbf{x}^{n-2}\mathbf{y}^2, \dots, \mathbf{x}, \mathbf{y}, \mathbf{1}].$$

Thus, we need at least $m \geq \frac{(n+2)(n+1)}{2}$ data points to estimate an n -degree polynomial. Typically, $m > n$, and thus the system is overdetermined and matrix \mathbf{U} is not square.

Householder reflections can then be used to compute an orthogonal-triangular factorization :

$$\mathbf{U}\mathbf{P} = \mathbf{Q}\mathbf{R}$$

where \mathbf{P} is a permutation, \mathbf{Q} is orthogonal and \mathbf{R} is upper triangular (see the function DGEQRF from LAPACK [24]). Since \mathbf{P} is a permutation, it is squared and invertible, and thus we can have:

$$\mathbf{U} = \mathbf{Q}\mathbf{R}\mathbf{P}^{-1}$$

Replacing \mathbf{U} at equation (C.1), we obtain:

$$\mathbf{Q}\mathbf{R}\mathbf{P}^{-1}\mathbf{c} = \mathbf{z}$$

Since \mathbf{Q} is orthogonal we can express the equation above as:

$$\mathbf{R}\mathbf{P}^{-1}\mathbf{c} = \mathbf{Q}^T\mathbf{z}$$

The solution \mathbf{c} is as follows:

$$\mathbf{c} = \mathbf{P}\mathbf{a}$$

where \mathbf{a} is the solution to the following linear system:

$$\mathbf{R}\mathbf{a} = \mathbf{Q}^T\mathbf{z}$$

This system can be solved very quickly since \mathbf{R} is upper triangular.

Nevertheless, since in this application we may be working with pixels, vectors $\mathbf{x}, \mathbf{y} \in [1, 512]$. This means that when fitting high-order polynomials matrix \mathbf{U} will be very decompensated, and thus the algorithm will have problems of numerical stability. A way of reducing this shortcoming is to scale the columns of \mathbf{U} prior to the factorization, and afterwards to re-scale the obtained coefficients of \mathbf{c} .

Bibliography

- [1] R.H. Bartels, J.C. Beatty, and B.A. Barsky. *An Introduction to Splines for use in Computer Graphics & Geometric Modeling*. Morgan Kaufmann Publishers.
- [2] J. Beier, H. Oswald, and E. Fleck. Edge detection for coronary angiograms: Error correction and impact of derivatives. In *Proc. IEEE Computers in Cardiology*, pages 513–516, 1991.
- [3] A. Blake and M. Isard. *Active Contours: the application of techniques from graphics, vision, control theory and statistics to visual tracking of shapes in motion*. Springer-Verlag London Limited, 1998.
- [4] G. Borgefors. Distance transformations in arbitrary dimensions. *Comp. Graph. Imag. Proc.*, pages 321–345, 1984.
- [5] S. Bougnoux. From projective to euclidean space under any practical situation, a criticism of self-calibration. In *Proc. Sixth Internatinal Conf. Computer Vision*, pages 790–796, Jan. 1998.
- [6] D.C. Brown. Close-range camera calibration. *Photogrammetric Eng.*, 37(8):855–866, 1971.
- [7] C. Cañero and P. Radeva. Predictive (un)distortion model for 3D reconstruction purposes. Technical Report 61, Computer Vision Center, 2002.
- [8] C. Cañero, P. Radeva, R. Toledo, J.J. Villanueva, and J. Mauri. 3D curve reconstruction by biplane snakes. In *Proc. IEEE of ICPR*, volume 4, pages 563–566, 2000.
- [9] C. Cañero, F. Vilariño, J. Mauri, and P. Radeva. Predictive (un)distortion model and 3D reconstruction by biplane snakes. *IEEE Trans. Med. Imag.*, to appear, September 2002.
- [10] C. Cañero, F. Vilariño, F. Nofrerías, J. Mauri, and P. Radeva. Modelling the acquisition geometry of a C-arm angiography system for 3D reconstruction. *Lecture Notes in Computer Science*, to appear, September 2002.
- [11] B. Caprile and V. Torre. Using vanishing points for camera calibration. *Int. J. Comp. Vis.*, 4(2):127–140, Mar. 1990.

- [12] S.Y. Chen and J. Carroll. Three-dimensional reconstruction of coronary arterial tree based on biplane angiograms. In *SPIE. Medical Imaging: Image Processing*, volume 2710, Newport Beach, California, February 1996.
- [13] S.Y.J. Chen and C.E. Metz. Improved determination of biplane imaging geometry from two projection images and its application to three-dimensional reconstruction of coronary arterial trees. *Medical Physics*, 25(5):633–654, May 1997.
- [14] L.D. Cohen. On active contour models and ballons. *CVGIP: Imag. Under.*, 53(2):211–218, 1991.
- [15] J. Comín, J. Mauri, B. García, E. F-Nofrerías, J.A. Gómez, E. Iràculis, C. Quiles, F. Jara, A. Cequier, E. Esplugas, C. Cañero, P. Radeva, R. Toledo, and J. Villanueva. Selecció de l'estent en base a la longitud real de la lesió: un nou mètode. *Revista de la Societat Catalana de Cardiologia*, 1999.
- [16] T.F. Cootes, C.J. Taylor, D.H. Cooper, and J. Graham. Training models of shape from sets of examples. In *Proc. British Machine Vision Conference*, pages 9–18. Springer-Verlag, 1992.
- [17] E. Coste, D. Gibon, and J. Rousseau. Assessment of image intensifier and distorsion for DSA localization studies. *The British Journal of Radiology*, 70:70–73, 1997.
- [18] P.E. Danielsson. Euclidean distance mapping. *Comp. Graph. Imag. Proc.*, 14:227–248, 1980.
- [19] H. Delingette. Simplex meshes: a general representation for 3d shape reconstruction. Technical Report TR-2214, INRIA, Sophia-Antiopolis, France, 1994.
- [20] F. Devernay and O. Faugeras. Automatic calibration and removal of distorsion from scenes of structured environments. In *SPIE, Medical Imaging: Image Processing*, volume 2567, San Diego, CA, July 1995.
- [21] P-A. Dorsaz, Lidia Dorsaz, and P-A. Doriot. The effect of image distortion on 3-D reconstruction of coronary bypass grafts from angiographic views. *IEEE Trans. Med. Imag.*, 19(7), July 2000.
- [22] A.C.M. Dumay, J.H.C. Reiber, and J.J. Gerbrands. Determination of optimal angiographic viewing angles: Basic principles and evaluation study. *IEEE Trans. Med. Imag.*, 13(1), March 1994.
- [23] A. Wahle et al. Assessment of diffuse coronary artery disease by quantitative analysis of coronary morphology based upon 3-D reconstruction from biplane angiograms. *IEEE Trans. Med. Imag.*, 14(2):230–241, June 1995.
- [24] E. Anderson et al. *LAPACK User's Guide*. SIAM, Philadelphia, third edition, 1999.

- [25] E. Kerrien et al. Machine precision assessment for 3D/2D digital subtracted angiography images registration. In *SPIE, Medical Imaging, Image Processing*, volume 3338, San Diego, California, February 1998.
- [26] H. Wollschläger et al. Improvement of quantitative angiography by exact calculation of radiological magnification factors. In *Computers in Cardiology*, pages 483–486, 1985.
- [27] J.H.C. Reiber et al. Coronary artery dimensions from cineangiograms—methodology and validation of a computer-assisted analysis procedure. *IEEE Trans. Med. Imag.*, 3:131–140, 1984.
- [28] K.R. Hoffmann et al. Determination of 3D positions of pacemaker leads from biplane angiographic sequences. *Medical Physics*, 24(12):1854–1862, December 1997.
- [29] L. Launay et al. Quantitative evaluation fo an algorithm for correcting geometrical distortions in DSA images: applications to stereotaxy. In *SPIE*, volume 2434, pages 520–529, San Diego, California, February 1995.
- [30] N. Ezquerra, S. Capell, L. Klein, and P. Duijves. Model-guided labeling of coronary structure. *IEEE Trans. Med. Imag.*, 17(3):429–441, June 1998.
- [31] W. Faig. Calibration of close-range photogrammetry systems: Mathematical formulation. *Photogrammetric Eng. and Remote Sensing*, 41(12):1479–1486, 1975.
- [32] O. Faugeras. *Three-Dimensional Computer Vision: A Geometric Viewpoint*. The MIT Press, 1993.
- [33] G.L. Flynn. Mass transport phenomena and models: Theoretical concepts. *J. Pharm. Sci.*, 63(4):479–510, 1974.
- [34] A.F. Frangi, W.J. Niessen, K.L. Vincken, and M.A. Viergever. Multiscale vessel enhancement filtering. In *Proc. MICCAI'98. Lecture Notes in Computer Science*, volume 1496, pages 130–137. Springer-Verlag, 1998.
- [35] S. Ganapathy. Decomposition of transformation matrices for robot vision. *Pattern Recognition Letters*, 2:401–412, Dec. 1984.
- [36] M. Garreau, J.L. Coatrieux, R. Collorec, and C. Chardenon. A knowledge-based approach for 3-D reconstruction and labeling of vascular networks from biplane angiographic projections. *IEEE Trans. Med. Imag.*, 10(2):122–129, 1991.
- [37] H. Greenspan, M. Laifenfeld, S. Einav, and O. Barnea. Evaluation of center-line extraction algorithms in quantitative coronary angiography. *IEEE Trans. Med. Imag.*, 20(9):928–941, 2001.
- [38] E. Gronenschild. The accuracy and reproducibility of a global method to correct for geometric image distortion in the X-ray imaging chain. *Medical Physics*, 24(2):1875–1888, 1997.

- [39] R. Hartley. Self-calibration from multiple views with a rotating camera. In *Proc. Third European Conf. Computer Vision*, pages 471–478, May 1994.
- [40] R.I. Hartley. An algorithm for self-calibration from several views. In *Proc. IEEE Conf. Computer Vision and Pattern Recognition*, pages 908–912, June 1994.
- [41] B. Jähne. Spatio-temporal image processing. In *Lecture Notes in Computer Science*, volume 751, pages 143–152, Berlin/New York, June 1993. Springer-Verlag.
- [42] M. Kass, A. Witkin, and D. Terzopoulos. Snakes: Active contours using finite elements to control local shape. In *ICCV*, pages 259–268, 1987.
- [43] B.B. Kimia, A.R. Tannenbaum, and S.W. Zucker. Shapes, shocks, and deformations i: the components of two-dimensional shape and reaction-diffusion space. *Int. J. Comp. Vis.*, 15:189–224, 1995.
- [44] R. Kimmel, A. Amir, and M. Bruckstein. Finding shortest paths on surfaces using level sets propagation. *IEEE Trans. Patt. Anal. Mach. Intell.*, 17(6):635–640, 1995.
- [45] K. Kitamura, J.M. Tobis, and J. Sklansky. Estimating the 3-D skeletons and transverse areas of coronary arteries from biplane angiograms. *IEEE Trans. Med. Imag.*, 7(3):173–187, September 1988.
- [46] J.J. Koenderink and A.J. van Doorn. Dynamic shape. *Biol. Cyber.*, 53:367–375, 1986.
- [47] D. Liebowitz and A. Zisserman. Metric rectification for perspective images of planes. In *Proc. IEEE Conf. Computer Vision and Pattern Recognition*, pages 482–488, June 1998.
- [48] T. Lindeberg. Edge detection and ridge detection with automatic scale selection. In *Proc. Conf. on Comp. Vis. and Pat. Recog.*, pages 465–470, June 1996.
- [49] C. Lorenz, I.-C. Carlsen, Buzug T.M., C. Fassnacht, and J. Weese. Multi-scale line segmentation with automatic estimation of width, contrast and tangential direction in 2d and 3d medical images. In *Proc. CVRMed-MRCAS'97. Lecture Notes in Computer Science*, volume 1205, pages 233–242. Springer-Verlag, 1997.
- [50] A. M. López, R. Toledo, J. Serrat, and J. J. Villanueva. Extraction of vessel centerlines from 2d coronary angiographies. In M.I. Torres and A. Sanfeliu, editors, *Proc. SNRF AI'99*, volume I, pages 489–496. Ediciones Geneve, 1999.
- [51] A.M. López, R. Toledo, J. Serrat, and J.J. Villanueva. Extraction of vessel centerlines from 2D coronary angiographies. In M.I. Torres and A. Sanfeliu, editors, *Proc. of SNRF AI*, volume I, pages 489–496, Bilbao (Spain), June 1999. Ediciones Geneve.
- [52] Q.-T. Luong. *Matrice Fondamentale et Calibration Visuelle sur l'Environnement-Vers une plus Grande Autonomie des Systèmes Robotiques*. PhD thesis, Université de Paris-Sud, Centre d'Orsay, Dec 1992.

- [53] Q.-T. Luong and O. Faugeras. Self-calibration of a moving camera from point correspondences and fundamental matrices. *Photogrammetric Eng. and Remote Sensing*, 22(3):261–289, 1997.
- [54] D. MacDonald, D. Avis, and A.C. Evans. Multiple surface identification and matching in magnetic resonance images. In *SPIE Proc. Visualization in Biomedical Computing*, volume 2359, pages 160–169, 1994.
- [55] J. Mauri, E. Nofrerías, A. Tovar, E. Martínez, L. Cano, C. Julià, V. Valle, D. Rotger, C. Cañero, and P. Radeva. Ecografia intracoronària: un nou pas, la fusió d'imatges amb l'angiografia, el software. *Revista de la Societat Catalana de Cardiologia*, 2434(1):48, 2001.
- [56] S.J. Maybank and O.D. Faugeras. A theory of self-calibration of a moving camera. *Int. J. Computer Vision*, 8(2):123–152, Aug. 1992.
- [57] T. McInerney and D. Terzopoulos. Deformable models in medical image analysis: A survey. *Medical Image Analysis*, 1(2):91–108, 1996.
- [58] E. Meijering. *Image Enhancement in Digital X-Ray Angiography*. PhD thesis, University Medical Center Utrecht, Oct 2000.
- [59] E.H.W. Meijering, W.J. Niessen, and M.A. Viergever. Retrospective motion correction in digital subtraction angiography: a review. *IEEE Trans. Med. Imag.*, 18(1):2–21, Jan. 1999.
- [60] S. Menet, P. Saint-Marc, and G. Medioni. The calibration problem for stereo. In *Proc. IEEE Conf. Computer Vision and Pattern Recognition*, pages 15–20, June 1986.
- [61] S. Menet, P. Saint-Marc, and G. Medioni. B-snakes: Implementation and application to stereo. In *DARPA Image Understanding Workshop*, pages 720–726, September 1990.
- [62] C.E. Metz and L.E. Fencil. Determination of three-dimensional structure in biplane radiography without prior knowledge of the relationship between the two views: Theory. *Medical Physics*, 16:45–51, 1990.
- [63] M.M. Mitschke and N. Navab. Optimal configuration for dynamic calibration of projection geometry of X-ray C-arm systems. In *Proc. of MMBIA*, pages 204–209, June 2000.
- [64] C. Molina, G.P. Prause, P. Radeva, and M. Sonka. Catheter path reconstruction from biplane angiography using 3D snakes. In *SPIE. Medical Imaging. Image Processing*, February 1998.
- [65] L. Alvarez nad F. Guichard, P.L. Lions, and J.M. Morel. Axioms and fundamental equations of image processing. *Archive for Rational Mechanics and Analysis*, 13(3):199–257, 1993.

- [66] E.F. Nofrerías, J. Mauri, J. Comín, B. García del Blasco, E. Iráculis, J.A. Gómez Hospital, P. Valdovinos, F. Jara, A. Cequier, E. Esplugas, C. Cañero, O. Pujol, D. Gil, R. Radeva, R. Toledo, and J. Villanueva. Selecció de l'stent en base a la longitud real de la lesió: l'entorn informàtic. *Revista de la Societat Catalana de Cardiologia*, June 2000.
- [67] D.G.W. Onnasch and G.P.M. Prause. Geometric image correction and iso-center calibration at oblique biplane angiographic views. In *Proc. IEEE Computers in Cardiology*, pages 647–650, 1992.
- [68] S. Osher and J.A. Sethian. Fronts propagating with curvature-dependent speed: algorithms based on hamilton-jacobi formulations. *J. Computational Physics*, 79:12–49, 1988.
- [69] N. Otsu. A threshold selection method from gray-level histograms. *IEEE Transactions on Systems, Man and Cybernetics*, 9(1):62–66, 1979.
- [70] N. Otsu. A threshold selection method from gray-level histograms. *IEEE Trans. Syst., Man, Cybern.*, 9(1):62–66, 1979.
- [71] Xavier Pennec. Computing the mean of geometric features. Application to the mean rotation. Technical report, INRIA, March 1998. Available at <http://www-sop.inria.fr/rappports/sophia/RR-3371.html>.
- [72] P. Perona and J. Malik. Scale-space and edge detection using anisotropic diffusion. *IEEE Trans. Pattern Anal. Mach. Intell.*, 12:629–639, 1990.
- [73] O. Pujol, C. Cañero, P. Radeva, R. Toledo, D. Gil, J. Saludes, J. J. Villanueva, B. Garcia del Blanco, J. Mauri, E. F. Nofrerías, J. A. Gómez-Hospital, E. Iràculis, J. Comín, C. Quiles, F. Jara, A. Cequier, and E. Esplugas. Three-dimensional reconstruction of coronary tree using intravascular ultrasound images. In *Proc. IEEE Computers in Cardiology*, pages 265–268, 1999.
- [74] O. Pujol, C. Cañero, P. Radeva, R. Toledo, J. Saludes, D. Gil, J.J. Villanueva, J. Mauri, B. García, J. Gómez, A. Cequier, and E. Esplugas. Three-dimensional reconstruction and quantification of the coronary tree using intravascular ultrasound images. In *IEEE Proc. of Computers in Cardiology*, volume 26, pages 265–268, Hannover, Germany, September 1999.
- [75] P. Radeva. *Model-Based Deformable Shapes for Segmentation, Registration and Tracking*. PhD thesis, Universitat Autònoma de Barcelona, July 1996.
- [76] D.A. Reimann and M.J. Flynn. Automated distortion correction of X-ray image intensifier images. In *IEEE Nuclear Science Symposium and Medical Imaging Conference Record*, pages 1339–1341, Orlando, Florida, October 1992.
- [77] D. Rotger. Multimodal registration of intravascular ultrasound images and angiography. Master's thesis, Universitat Autònoma de Barcelona, September 2002.

- [78] D. Rotger, P. Radeva, C. Cañero, J.J. Villanueva, J. Mauri, E. Fernández-Nofrerías, A. Tovar, and V. Valle. Corresponding IVUS and angiogram image data. In *Proc. of Computers in Cardiology*, volume 28, pages 273–276, Rotterdam, The Netherlands, September 2001.
- [79] D. Rotger, P. Radeva, C. Cañero, J.J. Villanueva, J. Mauri, E. Fernández-Nofrerías, A. Tovar, and V. Valle. Corresponding IVUS and angiogram image data. In *IEEE Proc. of Computers in Cardiology*, volume 28, pages 273–276, Rotterdam, The Netherlands, September 2001.
- [80] G. Sapiro and A. Tannenbaum. Affine invariant scale-space. *Int. J. Comp. Vis.*, 11(1):25–44, 1993.
- [81] Y. Sato, S. Nakajima, H. Atsumi, T. Koller, G. Gerig, S. Yoshida, and R. Kikinis. 3D multi-scale line filter for segmentation and visualization of curvilinear structures in medical images. In *Proc. CVRMed-MRCAS'97, LNCS*, pages 213–222, 1997.
- [82] J.A. Sethian. *Level Set Methods and Fast Marching Methods: Evolving Interfaces in Computation Geometry, Fluid Mechanics, Computer Vision, and Material Science*. Cambridge University Press, Cambridge, UK, 2nd edition, 1999.
- [83] J. Sigbers. *Signal and Noise Estimation from Magnetic Resonance Images*. PhD thesis, Universitaire Instelling Antwerpen, 1998.
- [84] C. Smets, F. van de Werf, P Suetens, and A. Oosterlinck. An expert system for the labeling and 3D reconstruction of the coronary arteries from two projections. *International Journal of Cardiac Imaging*, 5:145–154, 1990.
- [85] A.F. Solé, A. López, and G. Sapiro. Crease enhancement diffusion. *Comput. Vision and Image Understanding*, 84:241–248, 2001.
- [86] G. Stein. Accurate internal camera calibration using rotation, with analysis of sources of error. In *Proc. Fifth International Conf. Computer Vision*, pages 230–236, June 1995.
- [87] P.F. Sturm and S.J. Maybank. On plane-based camera calibration: A general algorithm, singularities, applications. In *Proc. of CVPR*, pages 432–437, Fort Collins, Colorado, June 1999.
- [88] H. Tek and B.B. Kimia. Volumetric segmentation of medical iamges by three-dimensional bubbles. *Comp. Vis. Imag. Under.*, 65:246–258, 1997.
- [89] D. Terzopoulos. On matching deformable models to images. Technical Report 60, Schlumberger Palo Alto Research, 1986.
- [90] R. Toledo. *Cardiac Workstation and Dynamic Model to Assist in Coronary Tree Analysis*. PhD thesis, Universitat Autònoma de Barcelona, July 2001.
- [91] R.Y. Tsai. A versatile camera calibration technique for high-accuracy 3D machine vision metrology using off-the-shelf TV cameras and lenses. *IEEE J. Robotics and Automation*, 3(4):323–344, August 1987.

- [92] C.D. von Land. Management and communication of digital x-ray angiographic image sequences. Master's thesis, Universitat Autònoma de Barcelona, June 1998.
- [93] A. Wahle, G. Prause, S. DeJong, and M. Sonka. Geometrically correct 3-D reconstruction of intravascular ultrasound images by fusion with biplane angiography - methods and validation. *IEEE Trans. Med. Imag.*, 18(8):686–699, August 1999.
- [94] W. Wahle, H. Oswald, G.A. Schulze, J. Beier, and E. Fleck. 3-d reconstruction, modelling and viewing of coronary vessels. In *CAR'91*, pages 669–676, 1991.
- [95] J. Weickert. *Anisotropic diffusion in image processing*. ECMI Series. Teubner, 1998.
- [96] J. Weng, P. Cohen, and M. Herniou. Camera calibration with distortion models and accuracy evaluation. *IEEE Trans. Pattern Analysis and Machine Intelligence*, 14(10):965–980, Oct. 1992.
- [97] A.P. Witkin. Scale-space filtering. In *Proc. International Joint Conference on Artificial Intelligence*, pages 1019–1021, 1983.
- [98] W. Wunderlich, F. Fischer, H.-R. Arntz, H.-P. Schultheiss, and A.J. Morguet. Development and clinical evaluation of an online procedure for lesion length measurement in coronary intervention. In *CIC'99*, September 1999.
- [99] C. Xu, D. L. Pham, and J. L. Prince. *Handbook of Medical Imaging – Volume 2: Medical Image Processing and Analysis*, chapter Medical Image Segmentation Using Deformable Models, pages 129–174. SPIE Press, May 2000. edited by J.M. Fitzpatrick and M. Sonka.
- [100] C. Xu and J.L. Prince. Generalized gradient vector flow external forces for active contours. *Signal Processing*, 71:131–139, 1998.
- [101] C. Xu and J.L. Prince. Snakes, shapes and gradient vector flow. *IEEE Trans. Image Processing*, 7(3):359–369, March 1998. MATLAB code available at <http://iacl.ece.jhu.edu/projects/gvf/>.
- [102] G. Xu and Z. Zhang. *Epipolar Geometry in Stereo, Motion and Object Recognition. A Unified Approach.*, volume 6 of *Computational Imaging and Vision*. Kluwer Academic Publishers, 1996.
- [103] Z. Zhang. A flexible new technique for camera calibration. *IEEE Trans. Pattern Anal. Machine Intell.*, 22(11):1330–1334, November 2000.
- [104] Z. Zhang, R. Deriche, O. Faugeras, and Q.-T. Luong. A robust technique for matching two uncalibrated images through the recovery of the unknown epipolar geometry. *Artificial Intelligence Journal*, 78:87–119, 1995.

Publications

- C. Cañero, F. Vilariño, J. Mauri and P. Radeva. "Predictive (un)distortion model and 3D Reconstruction by Biplane Snakes." *IEEE Transactions on Medical Imaging* (in press)
- C. Cañero, E. Nofrerías, J. Mauri and P. Radeva. "Modelling the acquisition geometry of a C-arm angiography system for 3D reconstruction". *Lecture Notes in Artificial Intelligence*. (in press)
- D. Rotger, P. Radeva, C. Cañero, JJ Villanueva, J. Mauri, E. Nofrerías, A. Tovar, V. Valle, "Advanced Visualization of 3D Data of Intravascular Ultrasound Images", *Lecture Notes in Computer Science*, October, 2001

- Rotger, Radeva, Cañero, Villanueva, Mauri, Fernández-Nofrerías, Tovar, Valle, "Corresponding IVUS And Angiogram Image Data", *Proceedings of Computers in Cardiology*, 28:273-276, Rotterdam, The Netherlands, September 2001.
- P. Radeva, C. Cañero, J.J. Villanueva, J. Mauri, E. Nofrerías, "3D Reconstruction of a Stent by Deformable Models", *Proceedings of the IASTED International Conference, Visualization, Imaging and Image Processing*, pp. 477-422, 2001.
- D. Rotger, C. Cañero, P. Radeva, J. Mauri, E. Fernández, A. Tovar, V. Valle, "3D Interactive Visualization and Volumetric Measurements of Coronary Vessels in IVUS", *Proceedings of the IX Spanish Symposium on Pattern Recognition and Image Analysis*, 1:151-156, 2001.
- J. Mauri, E. Nofrerías, A. Tovar, E. Martínez, L. Cano, C. Julià, V. Valle, D. Rotger, C. Cañero, P. Radeva, "Ecografia intracoronària: un nou pas, la fusió d'imatges amb l'angiografia, el software", *Revista de la Societat Catalana de Cardiologia* Vol 4 Supplement 1, 2001:48.
- C. Cañero, P. Radeva, R. Toledo, J.J. Villanueva, J. Mauri, "3D Curve Reconstruction by Biplane Snakes". *Proceedings of International Conference on Pattern Recognition (ICPR)*. September 2000.
- R. Toledo, X. Orriols, P. Radeva, X. Binefa, J. Vitrià, C. Cañero, J. Villanueva. "Eigensnakes for Vessel Segmentation in Angiography". *Proceedings of International Conference on Pattern Recognition (ICPR)*. September 2000.

- C. Cañero. "Models deformables aplicats a imatges mèdiques". *Master Thesis*. Universitat Autònoma de Barcelona (UAB). July 2000.
- E.F. Nofrerías, J. Mauri, J. Comín, B. García del Blasco, E. Iráculis, J.A. Gómez Hospital, P. Valdovinos, F. Jara, A. Cequier, E. Esplugas, C. Cañero, O. Pujol, D. Gil, R. Radeva, R. Toledo, J. Villanueva. "Selecció de l'Stent en base a la Longitud Real de la Lesió: l'Entorn Informàtic". *Revista de la Societat Catalana de Cardiologia*. Barcelona, June 2000.
- J. Mauri, E. F. Nofrerías, B. García, E. Iráculis, J. A. Gómez, J. Comín, M. A. Sánchez, F. Jara, A. Cequier, E. Esplugas, D. Gil, O. Pujol, C. Cañero, R. Radeva, R. Toledo, J. Villanueva. "Moviment del Vas en l'Anàlisi de les Imatges d'Ecografia Intracoronària: un Model Matemàtic". *Revista de la Societat Catalana de Cardiologia*. June 2000.
- J. Mauri, E. F. Nofrerías, J. Comín, B. García, E. Iráculis, J. A. Gómez, P. Valdovinos, F. Jara, A. Cequier, E. Esplugas, O. Pujol, C. Cañero, D. Gil, R. Radeva, R. Toledo, J. Villanueva. "Avaluació del Conjunt Stent/Artèria mitjançant Ecografia Intracoronària: L'Entorn Informàtic". *Revista de la Societat Catalana de Cardiologia*. June 2000.
- C. Cañero, O. Pujol, P. Radeva, et al. "Optimal Stent Implantation: Three-dimensional Evaluation of the Mutual Position of Stent and Vessel via Intracoronary Ecography". *Proceedings of International Conference on Computers in Cardiology*, Hannover, 1999.
- O. Pujol, P. Radeva, C. Cañero et al. "Three-dimensional reconstruction and quantification of the coronary tree using intravascular ultrasound images". *Proceedings of International Conference on Computers in Cardiology*, Hannover, 1999.
- Cristina Cañero. "Deformable Models applied in Medical Imaging". *Technical Report*, 33, Computer Vision Center, September 1999.
- J. Comín, J. Mauri, B. García, E. F. Nofrerías, J.A. Gómez, E. Iráculis, C. Quiles, F. Jara, A. Cequier, E. Esplugas, C. Cañero, P. Radeva, R. Toledo, J. Villanueva, "Selecció de l'Stent en base a la longitud real de la lesió: un nou mètode". *Revista de la Societat Catalana de Cardiologia*, 1999.
- B. García, J. Mauri, E. F. Nofrerías, J.A. Gómez, E. Iráculis, J. Comín, C. Quiles, F. Jara, A. Cequier, E. Esplugas, O. Pujol, C. Cañero, P. Radeva, R. Toledo, J. Villanueva, "Implantació òptima d'stents: Avaluació tridimensional del conjunt stent/artèria mitjançant ecografia intracoronària", *Revista de la Societat Catalana de Cardiologia*, 1999.
- A. Solé, A. López, C. Cañero, P. Radeva, J. Saludes, "Crease enhancement diffusion", *Proceedings of the VIII Symposium Nacional de Reconocimiento de Formas y Análisis de Imágenes*, Bilbao, Spain, Vol.1, pp.279-286, 1999.

- D. Ponsa, A. Solé, A. López, C. Cañero, J. and P. Radeva. "Regularized EM". *Proceedings of the VIII SNRFAI*, Bilbao 1999. Vol. 1 pag. 3-10.

Curriculum Vitae



The author was born on May 21, 1976 in Terrassa, Spain. In the period 1990-1994 she received secondary education at the IES Nicolau Copèrnic, Terrassa, Spain, from which she obtained the High School leaving certificate (first class with honors) in 1994.

In the same year, she successfully passed the university entrance examinations, and entered university at the Universitat Autònoma de Barcelona, Bellaterra, Spain, where she studied the undergraduate studies of Computer Science Engineering. In 1998 she was awarded by an Erasmus grant to study an abroad semester at the Université Paris VIII in Paris, France. There she did her BSc thesis, and participated in the Robocup'98 (Robotic Soccer World Competition).

After graduating in June 1998, she started her MSc studies. From September 1998 to December 1998, she worked as assistant professor in the Unitat de Processament d'Imatges of the Departament d'Informàtica (UAB), teaching practical courses on Computer Graphics, mainly OpenGL. In January 1999, she was awarded a pre-doctoral grant by the Generalitat de Catalunya, which she received during the period 1999-2002. During this period, she worked on two research projects concerning the information extraction from X-ray angiography and IVUS images. She also continued teaching practical courses of Computer Graphics at the UAB. In September 2000, she received a MSc degree in Computer Vision from the Universitat Autònoma de Barcelona.

She has been selected for a Marie Curie Post-Doctoral fellowship by the European Community, to carry out research at the Informatics and Telematics Institute in Thessaloniki, Greece, starting in January 2002.